Atmospheric Boundary Layers over an Oceanic Eddy

PETER P. SULLIVAN[a] AND JAMES C. MCWILLIAMS[b]

[a] *National Center for Atmospheric Research, Boulder, Colorado*
[b] *Department of Atmospheric and Oceanic Sciences, University of California, Los Angeles, Los Angeles, California*

(Manuscript received 26 January 2022, in final form 21 May 2022)

ABSTRACT: Imagery and numerical modeling show an abundance of submesoscale oceanic eddies in the upper ocean. Large-eddy simulation (LES) is used to elucidate eddy impacts on the atmospheric boundary layer (ABL) forced by winds, convection, and an eddy with varying radius; the maximum azimuthal eddy speed is 1 m s^{-1}. Simulations span the unstable regime $-1/L = [0, \infty]$, where L is the Monin–Obukhov (M–O) stability parameter. A linearized Ekman model and the LES couple ABL winds to an eddy through rough-wall M–O boundary conditions. The eddy currents cause a surface stress anomaly that induces Ekman pumping in a dipole horizontal pattern. The dipole is understood as a consequence of surface winds aligned or opposing surface currents. In free convection a vigorous updraft is found above the eddy center and persists over the ABL depth. Heterogeneity in surface temperature flux is responsible for the full ABL impact. With winds and convection, current stress coupling generates a dipole in surface temperature flux even with constant sea surface temperature. Wind, pressure, and temperature anomalies are sensitive to an eddy under light winds. The eddy impact on ABL secondary circulations is on the order of the convective velocity scale w_* but grows with increasing current speed, decreasing wind, or increasing convection. Flow past an isolated eddy develops a coherent ABL "wake" and secondary circulations for at least five eddy radii downwind. Kinetic energy exchanges by wind work indicate an eddy-killing effect on the oceanic eddy current, but only a spatial rearrangement of the atmospheric wind work.

KEYWORDS: Atmosphere-ocean interaction; Boundary layer; Eddies; Large eddy simulations; Turbulence; Secondary circulation

1. Introduction

The conceptual paradigm for planetary boundary layers is horizontal homogeneity, and often stationarity as well. Besides embodying simplicity, these assumptions express a space- and time-scale separation between the boundary layer turbulence and the interior flow and the boundary characteristics. Yet these assumptions are often false in nature. In particular, the boundary itself need not be homogeneous, which is the focus of this paper.

The most important new dynamical element with inhomogeneity is three-dimensional secondary circulations (SCs), also called standing eddies, that can extend throughout the boundary layer from the surface to the inversion layer adjacent to the vertical interior, and thereby also modulate the more familiar transient turbulent eddies. This behavior is relevant for both atmospheric and oceanic boundary layers. We are particularly concerned with inhomogeneities on intermediate scales, comparable to or somewhat larger than the boundary layer thickness. Random, smaller-scale surface irregularities can be considered as analogous to surface roughness in the momentum stress formula.

Previously we have examined the effect of sea surface temperature (SST) inhomogeneity in large-eddy simulations (LES) of a weakly convective atmospheric boundary layer (ABL) for configurations of a SST front and filament and for different geostrophic wind directions (Sullivan et al. 2020, 2021, hereafter S20 and S21, respectively). This is a thermodynamic ocean–atmosphere coupling effect through the surface heat flux. Here we examine the complementary effect of an inhomogeneous oceanic current acting through the surface stress, and the current has the idealized shape of an isolated circular eddy.

There is an extensive literature for the ABL above inhomogeneous surfaces, especially land-forms (e.g., Garratt 1992; Raasch and Harbusch 2001; Owinoh et al. 2005; Patton et al. 2005). Over the ocean SST gradients modulate the gravitational stability of the ABL and induce local changes in the surface wind, in particular at the oceanic mesoscale (~100 km horizontally) (Chelton et al. 2011); this in turn forces inhomogeneous Ekman pumping in the ocean and impacts plankton distributions Gaube et al. (2013, 2015). Surface current gradients modulate the surface stress (Seo et al. 2016; Renault et al. 2016). Its clearest effect is to extract kinetic energy from the mesoscale currents (i.e., "eddy killing"), but its influence has also been shown for larger-scale currents (Renault et al. 2019). The feedback on the ABL from these surface couplings is less well understood, but it seems clear that they can be significant in low and high winds (Edson et al. 2007; Chen et al. 2007; Minobe et al. 2008; Frenger et al. 2013); this is an active area of research (Robinson et al. 2019; Ayet et al. 2021).

Much of the previous coupled air–sea modeling has relied on single-column boundary layer parameterizations, rather than turbulence-resolving LES, as here. Furthermore, most of the documented interactions are at the oceanic mesoscale (~10–100 km). However, the oceanic surface is full of submesoscale currents and SST fronts and filaments (~0.1–10 km) McWilliams (2016, 2020), and their coupling effects have only

Supplemental information related to this paper is available at the Journals Online website: https://doi.org/10.1175/JAS-D-22-0019.s1.

Corresponding author: Peter P. Sullivan, pps@ucar.edu

DOI: 10.1175/JAS-D-22-0019.1

just begun to be explored (Renault et al. 2018); it is likely that significant impacts will continue to this smaller scale.

A framework for interpreting the consequences of stress inhomogeneity is uniform-density, rotating, laminar boundary layers. For swirling flows or a rotating-boundary, radial outflows or inflows occur near the surface that are closed by secondary circulations (e.g., Schlichting 1968; Rotunno 2013, 2014). In our LES the eddy current differs from solid-body rotation, the boundary layer is turbulent, and buoyancy effects are active. Nevertheless, in this article we also describe a linearized Ekman-layer flow model coupled to an oceanic eddy that helps guide the interpretation of the computational results.

The outline of the paper is as follows: An analytic model for Ekman-layer winds over an oceanic eddy is developed in section 2. The LES equations and setup of the LES experiments for varying stability are described in section 3. The coupling of the ABL with an oceanic eddy and the surface boundary conditions are described in section 4. Results with winds alone (no surface heating), free convection (no mean winds), and winds plus convection are discussed in three separate sections (sections 5, 6, and 7, respectively). Section 8 is a summary of the findings.

2. Ekman-layer winds over an oceanic eddy

A paradigm for the atmospheric boundary layer is the Ekman model. It has simple horizontal momentum and continuity balances:

$$f\hat{\mathbf{z}}\times\mathbf{u}^h=\partial_z(\nu\partial_z\mathbf{u}^h),$$
$$w=-\boldsymbol{\nabla}^h\cdot\int_0^z\mathbf{u}^h dz, \tag{1}$$

for $z\in[0,\infty]$, where $\hat{\mathbf{z}}$ is a unit vertical vector, $\mathbf{u}^h=(u,v)$ is the horizontal velocity, w is the vertical velocity with a surface boundary condition of $w(0)=0$, and f and ν are the Coriolis frequency and vertical eddy viscosity, respectively, both assumed constant. For our purposes we choose a surface stress boundary condition:

$$\nu\partial_z\mathbf{u}^h(0)=-\frac{1}{\rho_a}\boldsymbol{\tau}_s^h, \tag{2}$$

where ρ_a is the atmospheric density and $\boldsymbol{\tau}_s$ is the stress of the underlying ocean on the atmosphere above. The interior boundary condition is $\partial_z\mathbf{u}^h\to 0$ as $z\to\infty$. The problem is well posed as a function of z for any $\boldsymbol{\tau}_s(x,y,t)$.

As commonly done, we adopt a mixed real vector and complex scalar notation for the Ekman vertical profiles, where the complex scalar has the x and y components of the vector as its real and imaginary parts. In particular,

$$\mathbf{u}^h\leftrightarrow\mathcal{U}=u+iv\quad\text{and}\quad\frac{1}{\rho_a}\boldsymbol{\tau}_s\leftrightarrow\mathcal{T}. \tag{3}$$

With this notation, the relevant solution to (1)–(2) is

$$\mathcal{U}(z)=\sqrt{\frac{1}{f\nu}}\mathcal{T}e^{-i\pi/4}e^{\lambda z}+\mathcal{U}_g, \tag{4}$$

with $\lambda=\sqrt{f/\nu}\exp(-i3\pi/4)$ the complex vertical decay and rotation scale and $\mathcal{U}_g$ the vertically interior horizontal wind above the boundary layer (in complex scalar notation). Because the real part of λ is negative, the first term decreases with z, and because the imaginary part is negative, its velocity direction rotates clockwise while ascending (a.k.a. the Ekman spiral). The second term is a constant interior velocity, presumed in geostrophic balance with an interior pressure gradient. The surface wind is rotated clockwise relative to the surface stress by $\pi/4$. The complex notation facilitates recognizing the various vector directions. Additionally the horizontal transport is

$$\mathbf{V}=\int_0^\infty\mathbf{u}^h(z)dz\leftrightarrow\mathcal{V}=\frac{1}{f}\mathcal{T}e^{-i\pi/2}, \tag{5}$$

rotated clockwise by $\pi/2$ relative to the surface stress. From (1) it is related to the vertical velocity at the top of the boundary layer (aka Ekman pumping) by

$$w_e\equiv w(\infty)=-\boldsymbol{\nabla}^h\cdot\mathbf{V}. \tag{6}$$

Over an unmoving, horizontally homogeneous surface, a bulk formula expresses the surface stress in terms of a near-surface atmospheric velocity and a drag coefficient C_D:

$$\boldsymbol{\tau}_s=-\rho C_D|\mathbf{u}_a^h|\mathbf{u}_a^h, \tag{7}$$

and the associated friction velocity is $u_*=\sqrt{|\boldsymbol{\tau}_s|/\rho_a}$. This relation is rooted in the surface (Monin–Obukhov) layer, which is inconsistent with the Ekman model because it is related to a variable local eddy viscosity $\propto u_*z$. In LES solutions for the neutral layer using (7), the (x,y,t)-averaged value for boundary $\mathbf{u}_a^h$ is only modestly reduced in magnitude from $\mathbf{u}_g$ at the top of the layer and rotated slightly counterclockwise (i.e., by about $\phi_a=10°$ or 0.17 radians), see section 5. Thus, in fitting an Ekman solution to this LES we choose a stress of

$$\mathcal{T}=-u_*^2e^{i\phi_a}=u_*^2e^{i(\phi_a+\pi)} \tag{8}$$

for use in (4), with $u_*\propto|\mathbf{u}_g|$. We further fit the Ekman eddy viscosity by $\nu\propto u_*z_i$, where z_i is the boundary layer height, which in the LES solution is stratification limited by the interior inversion layer. As an example (Table 1), for $f=10^{-4}$ s^{-1}, $\mathbf{u}_g=5$ m s^{-1} to the east, and $z_i=310$ m, fitted Ekman parameters are $u_*=0.15$ m s^{-1} and $\nu=5$ m^2 s^{-1} so that the Ekman vertical decay scale $\sqrt{2\nu/f}$ is equal to z_i. Of course, this is only a gross fitting, because the Ekman model neglects the more realistic effects of a variable $\nu(z)$, buoyancy and advection. The orientations of these various quantities are shown in Fig. 1.

For a heterogeneous surface with an oceanic current $\mathbf{u}_o^h(x,y)$, the bulk stress law is based on the relative velocity with the adjacent air:

$$\boldsymbol{\tau}_s^h=-\rho_aC_D|\mathbf{u}_a^h-\mathbf{u}_o^h|(\mathbf{u}_a^h-\mathbf{u}_o^h). \tag{9}$$

Further simplify it with the assumption that $|\mathbf{u}_o^h|\ll|\mathbf{u}_a^h|$:

$$\boldsymbol{\tau}_s^h\approx-\rho_aC_D\left(|\mathbf{u}_a^h-\mathbf{u}_o^h|\mathbf{u}_a^h-|\mathbf{u}_a^h|\mathbf{u}_o^h\right). \tag{10}$$

TABLE 1. LES parameters for free convection, mixed shear–convective, neutral, and Ekman simulations where Free, Mixed, Neutral, and Ekman mark the simulation family, respectively. $\theta_{BC} = 0$ fixed SST and $\theta_{BC} = 1$ fixed q_*. Results from simulation f08 are in the supplementary material.

Case	(u_g, u_{10}) (m s^{-1})	Eddy type	r_m (km)	θ_{BC}	$L_x = L_y$ (km)	$(N_{x,y}, N_z)$	q_* (K m s^{-1})	z_i (m)	u_* (m s^{-1})	w_* (m s^{-1})	z_i/r_m
Free											
f01	(0, 0)	Cyclonic	0.4	0	10	(1536, 384)	0.0107	637	0.0047	0.613	1.59
f02	(0, 0)	Anticyclonic	0.4	0	10	(1536, 384)	0.0107	637	0.0036	0.612	1.59
f03	(0, 0)	Cyclonic	0.4	1	10	(1536, 384)	0.015	697	0.0040	0.707	1.74
f04	(0, 0)	—	—	0	10	(1536, 384)	0.0105	638	0.0044	0.610	—
f05	(0, 0)	—	—	1	10	(1536, 384)	0.0106	638	0.0038	0.605	—
f08	(0, 0)	Cyclonic	4	0	36.9	(3072, 320)	0.0104	654	0.0024	0.614	0.163
Mixed											
i02	(2.5, 2.21)	Cyclonic	1.2	0	10	(1536, 384)	0.0128	715	0.0963	0.677	0.595
i03	(2.5, 2.20)	Cyclonic	2	0	10	(1536, 384)	0.0129	706	0.0966	0.676	0.353
i04	(2.5, 2.20)	—	—	0	10	(1536, 384)	0.0128	717	0.0957	0.676	—
i05	(2.5, 2.22)	Cyclonic	4	0	20	(3072, 384)	0.0127	730	0.0971	0.679	0.182
i06	(2.5, 2.18)	Anticyclonic	4	0	20	(3072, 384)	0.0130	692	0.0960	0.673	0.173
i07	(5, 4.43)	Cyclonic	4	0	20	(3072, 384)	0.0118	699	0.1728	0.652	0.175
h01	(5, 4.32)	Cyclonic	0.4	0	10	(1536, 384)	0.0124	653	0.1690	0.650	1.63
h04	(5, 4.25)	Cyclonic	4	0	20	(3072, 384)	0.0216	753	0.1709	0.820	0.188
Neutral											
k01	(2.5, 2.09)	Cyclonic	4	1	20	(3072, 384)	0	280	0.0779	0	0.070
k03	(5, 4.06)	Cyclonic	4	1	20	(3072, 384)	0	324	0.151	0	0.081
k04	(5, 4.11)	Anticyclonic	4	1	20	(3072, 384)	0	321	0.151	0	0.081
Ekman											
m01	(5, 3.86)	Cyclonic	4	1	20	(1536, 256)	—	783	0.1454	—	0.196

As discussed above, an accurate representation of $\mathbf{u}_a^h \leftrightarrow \mathcal{U}_a$ is not available in an Ekman model, so we will use $\mathbf{u}_g^h$ rotated by ϕ_a, consistent with (8) above. The current is assumed to be a circular eddy with amplitude U_o (positive for a cyclone), radial shape $F(r)$, and radial size r_m; i.e., in cylindrical coordinates:

$$\mathbf{u}_o^h \leftrightarrow \mathcal{U}_o(r,\phi) = U_o F(r) e^{i(\phi+\pi/2)}. \tag{11}$$

A simple shape choice both here and for the LES problem, see section 4a, is

$$F(r) = \left(\frac{r}{r_m}\right)\exp\left[-\left(\frac{r}{r_m}\right)^2\right]. \tag{12}$$

After some manipulations, the resulting surface stress from (10) is

$$\mathcal{T}(r,\phi) \approx -u_*^2\{e^{i\phi_a} + \varepsilon F(r)[\sin(\phi-\phi_a)e^{i\phi_a} + e^{i(\phi-\pi 2)}]\}, \tag{13}$$

where $\varepsilon = U_o/U_g$ is a small parameter used to make this first-order approximation to (9). At leading order, this formula is the same as horizontally homogeneous (8), and at first order we see the inhomogeneous effects of the oceanic eddy $\propto U_o$. The first current term $\propto -\exp(i\phi_a)$ has its stress in the same direction as the average stress (Fig. 1), and the second term $\propto -\exp[i(\phi-\pi 2)] = \exp[i(\phi+\pi 2)]$ has its stress directed along the eddy current, hence its transport $\mathbf{V}$ outward from the eddy center for a cyclone, with downwelling in the eddy core, and vice versa for an anticyclone. Because of the imprecision in evaluating $\mathbf{u}_a$ in the bulk formula, we will not attempt to make an accurate estimate of the magnitude of the eddy-induced atmospheric circulation but rather focus on its spatial patterns; in terms of the parameters in Table 1 for the LES

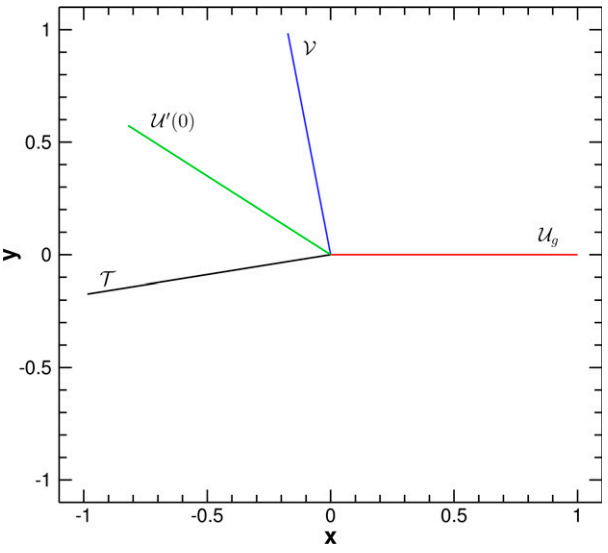

FIG. 1. A hodograph with interior wind $\mathcal{U}_g$ (red line), surface Ekman wind $\mathcal{U}'(0) = \mathcal{U}(0) - \mathcal{U}_g$ (green), surface stress $\mathcal{T}$ (black), and horizontal transport $\mathcal{V}$ (blue) as stick directions, based on the Ekman fit to a homogeneous neutral layer as described in the text. The relative orientations of the latter three directions are the same no matter what the $\boldsymbol{\tau}_s$ direction is.

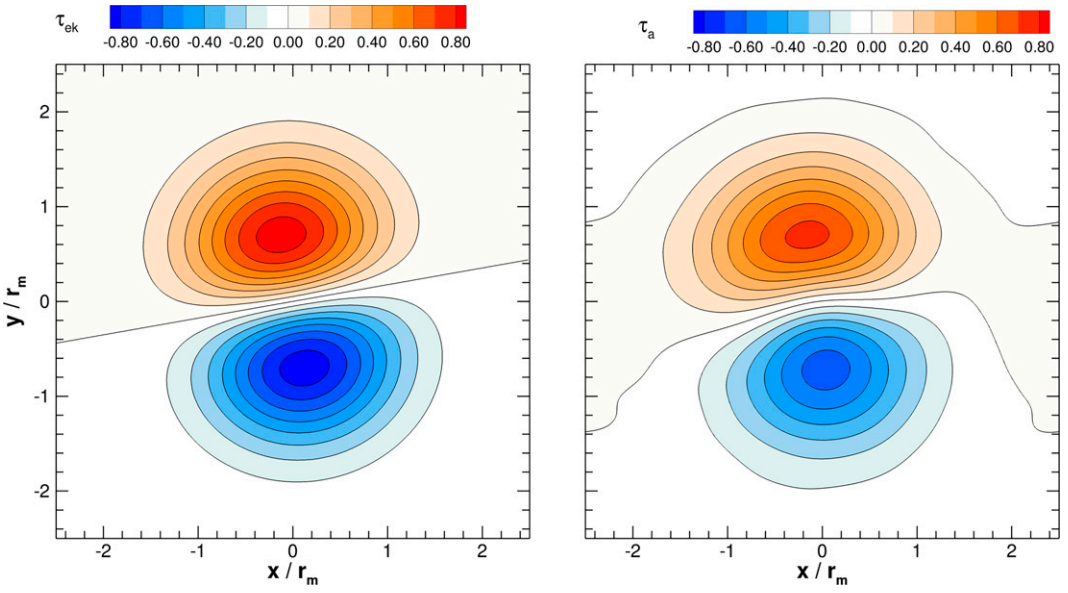

FIG. 2. (left) Eddy-induced anomaly in the surface momentum $|\mathcal{T}(x,y)|$ from (14). (right) LES surface momentum anomaly (21). The eddy is cyclonic in (11)–(12), and the geostrophic wind $\mathbf{u}_g^h = 5\,\mathrm{m\,s^{-1}}$ is eastward. The anomaly is normalized by ε.

cases with $u_g = 5$ m s^{-1}, $\varepsilon = 0.466$ with a maximum eddy current speed of 1 m s^{-1}.

The Ekman model is linear in its dependency on the different components of $\mathcal{T}$ in (13). Its magnitude is

$$|\mathcal{T}(r,\phi)| \approx u_*^2\,[1 + 2\varepsilon F(r)\sin(\phi - \phi_a)], \tag{14}$$

again retaining only terms first order in ε. Its spatial pattern is in Fig. 2 for a cyclonic eddy. Apart from the small counterclockwise rotation by ϕ_a, it is a dipole with enhanced stress to the north and reduced stress to the south. This is easily understood as a higher stress where the eddy current opposes the wind and a lower stress where it is in the wind direction.

The secondary circulation is most readily seen in the Ekman pumping velocity near the top of the boundary layer, $w_e(x, y)$ in (6). Using $\mathcal{T}$ from (13) to evaluate $\mathcal{V}$ from (5) and taking the horizontal divergence yields

$$w_e(r,\phi) = -\frac{u_*^2\varepsilon}{f}\left\{\partial_r F[1 + \sin^2(\phi - \phi_a)] + \frac{F}{r}[1 + \cos^2(\phi - \phi_a)]\right\}, \tag{15}$$

which is illustrated in Fig. 3 for a cyclonic eddy. The eddy core region has downwelling, consistent with horizontal transport divergence there. Furthermore, the exterior region has upwelling, and the area-integrated vertical transport is zero:

$$\int_0^{2\pi}\int_0^{\infty} w_e(r,\phi)\,r\,dr\,d\phi = 0. \tag{16}$$

The interior downwelling region extends further outward in the east–west direction, and there are local maxima in the exterior upwelling in the north–south direction. For an anticyclonic eddy, the Ekman model predicts a sign reversal for the w_e and $\mathcal{T}$ patterns.

In the absence of a mean interior wind, the surface stress is due entirely to the current:

$$\boldsymbol{\tau}_s^h = \rho_a C_D |\mathbf{u}_o^h| \mathbf{u}_o^h. \tag{17}$$

Its magnitude is $O(u_*^2\varepsilon^2)$, i.e., smaller than the eddy-induced stress anomaly when a mean wind is present. The stress direction is in the current direction. So, for a cyclone the eddy-induced transport is outward; and the Ekman pumping is downward in the eddy core and upward outside, again with zero area integral. For an anticyclone these patterns reverse in sign.

Finally, although the Ekman model has no buoyancy effects, we can anticipate that the bulk formula for surface heat flux, with $q_* \propto |\mathbf{u}_a^h - \mathbf{u}_o^h|$, will exhibit a similar anomaly pattern to the surface stress: with an eastward interior wind, a cyclonic eddy, and a warm oceanic surface, there is a positive flux anomaly to the north and a negative one to the south, and vice versa for an anticyclonic eddy. Without a mean interior wind, there is a positive q_* anomaly in a ring near $r = r_m$ for both cyclones and anticyclonic eddies because there is a positive stress magnitude anomaly for both.

3. LES details

a. LES equations

The LES equations and solution algorithm are briefly described in order to introduce the Cartesian coordinate system and variables used in the simulations and analysis. For completeness in describing the LES, we reintroduce variable definitions used in section 2. In the LES: $\mathbf{u} \equiv u_i = (u, v, w)$ denote the Cartesian velocity components, θ is virtual potential

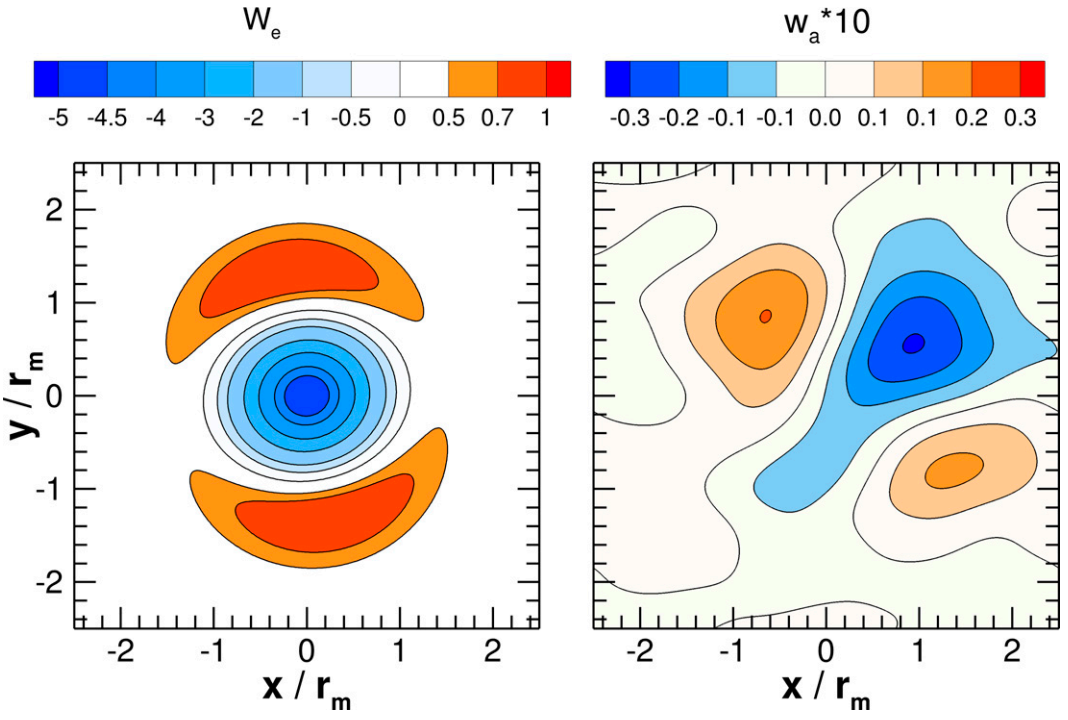

FIG. 3. (left) Eddy-induced Ekman pumping $w_e(x, y)$ from (6). (right) Vertical velocity w_a from case k03 at $z = 60.5$ m. The fields are normalized by $(u_*^2\varepsilon)/(fr_m)$, and the eddy rotation is cyclonic in an eastward $\mathbf{u}_g^h$ as in Fig. 1.

temperature and p is the pressure variable normalized by air density ρ_a. The three Cartesian coordinates are $\mathbf{x} \equiv x_i = (x, y, z)$ also referred to as (streamwise, spanwise, vertical) directions, respectively. The set of LES equations that describe rotating stratified turbulent flow in a ABL under the incompressible Boussinesq approximation are

$$\frac{\partial \mathbf{u}}{\partial t} = -\mathbf{u}\cdot\boldsymbol{\nabla}\mathbf{u} - \mathbf{f}\times(\mathbf{u}-\mathbf{u}_g) - \boldsymbol{\nabla}p + \hat{\mathbf{z}}\beta(\theta-\theta_r) - \boldsymbol{\nabla}\cdot\mathbf{T}, \tag{18a}$$

$$\frac{\partial \theta}{\partial t} = -\mathbf{u}\cdot\boldsymbol{\nabla}\theta - \boldsymbol{\nabla}\cdot\mathbf{B}, \tag{18b}$$

$$\boldsymbol{\nabla}\cdot\mathbf{u} = 0. \tag{18c}$$

The above equation set includes transport equations: for momentum $\rho_a\mathbf{u}$, (18a), and for virtual potential temperature, θ (18b); θ is referred to as "temperature" in the narrative. The divergence free (incompressible) condition (18c) determines the elliptic pressure variable p. Equation set (18) also includes: geostrophic winds $\mathbf{u}_g = (u_g, v_g)$, rotation vector $\mathbf{f} = (0, 0, f)$ with Coriolis parameter f, unit vector $\hat{\mathbf{z}}$ in the vertical direction, and buoyancy parameter $\beta = g/\theta_r$ where g is gravity and θ_r is the reference potential temperature. The subgrid-scale (SGS) momentum and temperature fluxes ($\mathbf{T}$, $\mathbf{B}$) are estimated using turbulent eddy viscosity prescriptions. Other details are found in S20 and S21.

b. Mesh resolution and data sampling

Four families of LES experiments with varying geostrophic winds, domain size, and surface boundary conditions are carried out: 1) free convection, 2) mixed shear and convection, 3) shear driven neutral, and 4) Ekman see Table 1. The simulations span the stability range $-z/L = [0, \infty]$, where z is the vertical coordinate and L is the Monin–Obukhov stability length. The LES setup including the number of grid points used for each type of simulation are listed in Table 1. The horizontal mesh resolution for all simulations is $\Delta(x, y) = 6.5$ m, except for the Ekman simulation where $\Delta(x, y) = 13$ m. The vertical mesh is a smoothly stretched grid built with a near unity stretching factor $K = \Delta z_{k+1}/\Delta z_k = 1.000\,99$. Here k is the vertical index, and the first vertical w grid point is located at $\Delta z_1 = 3$ m, (Fig. 5). The vertical domain is $L_z = 1.4$ km and is more than 2 times the final boundary layer depth z_i. It is convenient to position the origin of the horizontal coordinates (x, y) at the center of the LES domain: thus $x = [-L_x/2, L_x/2]$ and $y = [-L_y/2, L_y/2]$ where (L_x, L_y) denote the lengths of the horizontal domain.

All the simulations are started using the same recipe. First, a small domain LES (5, 5, 1.4) km with mesh points $(N_x, N_y, N_z) = (768, 768, 384)$ is run starting with random initial conditions, fixed temperature flux $q_* = 0.015$ K m s^{-1}, the desired geostrophic wind, and no eddy currents. These small domain simulations are run for approximately 30 000 steps until turbulence is fully developed. The last volume from the small domain LES is archived and replicated in x and y to span the larger domains in Table 1. At the same time the number of mesh points is increased, i.e., the mesh resolution is not changed. Finally the large domain fine mesh LES is started but now including the eddy currents. The simulations are run for approximately 30 000 additional steps. Data are analyzed

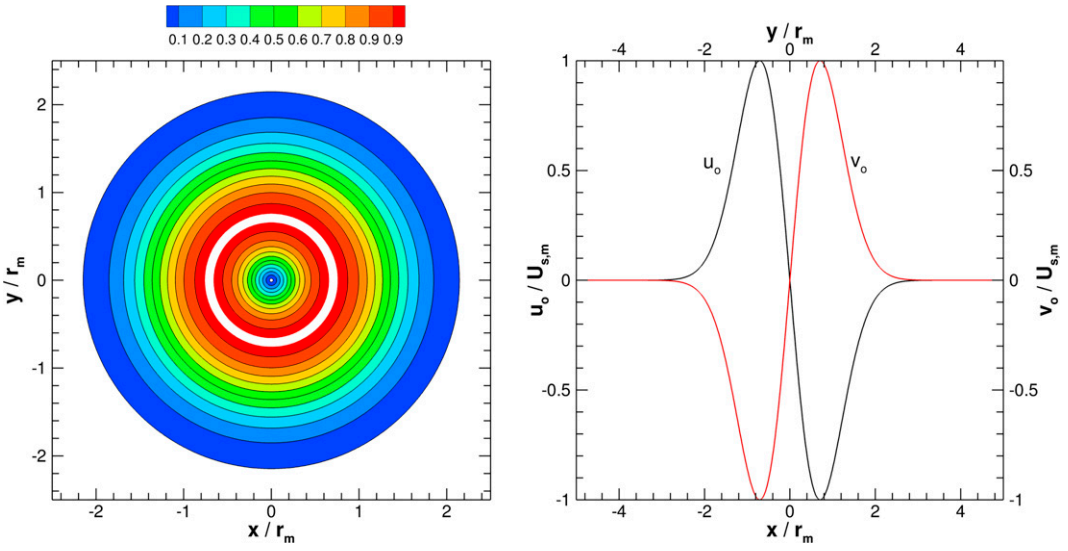

FIG. 4. (left) Contours of the eddy azimuthal current $U_s/U_{s,m}$. The white ring shows the location of the maximum current $U_{s,m} = 1$ m s^{-1}. (right) The Cartesian components $(u, v)_o$ of the azimuthal current normalized by $U_{s,m}$. The slices show the variation of u_o with y/r_m at $x = 0$ (black line) and the variation of v_o with x/r_m at $y = 0$ (red line).

over the last 2.8 h of the simulation when the fields are quasi-steady. Variables in Table 1 include the wind speed at the 10 m level u_{10}, friction velocity u_*, convective velocity scale w_* (Deardorff 1970), boundary layer depth z_i (Sullivan et al. 1998), temperature flux q_*, and characteristic eddy radius r_m. To expose the eddy induced motions we use low-pass filtering, specifically a Gaussian filter applied in spectral space with filter scale δ (e.g., Pope 2000, p. 563).

4. LES and current coupling

a. Oceanic eddy

As in section 2, we impose a single circular oceanic eddy at the bottom of the LES with radial shape $F(r)$ and azimuthal speed given by

$$U_s = U_o F(r) \equiv U_o(r/r_m)\exp[-(r/r_m)^2]. \tag{19}$$

In terms of polar coordinates (r, ϕ), the Cartesian components used in the LES are $(u_o, v_o) = U_s[-\sin(\phi), \cos(\phi)]$. The parameter U_o controls the eddy speed and rotational direction and r_m is a measure of the eddy width. The eddy speed U_s increases linearly with small r, i.e., with solid body rotation, and is exponentially damped in the far field. The eddy speed reaches a maximum $U_{s,m} = U_o\sqrt{1/2}\,e^{-1/2} \sim 0.429U_o$ at $r = \sqrt{(1/2)}\,r_m \sim 0.707r_m$. Figure 4 shows contours of U_s, normalized by the maximum current $U_{s,m} = 1$ m s^{-1}. To illustrate the symmetries of the circular eddy, Fig. 4 also shows the variation of the Cartesian velocity components $\mathbf{u}_o = (u_o, v_o)$ slicing through the eddy center; u_o for varying y/r_m at constant $x = 0$, and v_0 for varying x/r_m at constant $y = 0$. Note $(u_o < 0, u_o > 0)$ in the upper and lower halves of the vortex while $(v_o > 0, v_o < 0)$ in the right and left halves of the vortex. The sinusoidal oscillation of the (u_o, v_o) velocity components in the vortex has an important impact on the results. In all simulations the eddy center is located at $(x, y) = (0, 0)$. For the simulations in Table 1 the parameter $\varepsilon = U_o/u_g = [\infty, 0.932, 0.466[$, and $\varepsilon(>0, <0)$ for (cyclonic, anticyclonic) rotation.

b. Surface boundary conditions

Figure 5 illustrates the staggered vertical arrangement of flow variables at two levels above the water surface used to implement the surface boundary conditions in the LES. Variables (u, v, p, θ) are located at the $(z_{1/2}, z_{3/2})$-levels while variables (w, e) are located at the (z_1, z_2)-levels; the $(z_{1/2}, z_{3/2})$-levels are centered midway between the (z_1, z_2)-levels. We adopt rough-wall Monin–Obukhov (M–O) similarity formulas for the calculation of momentum and temperature fluxes at

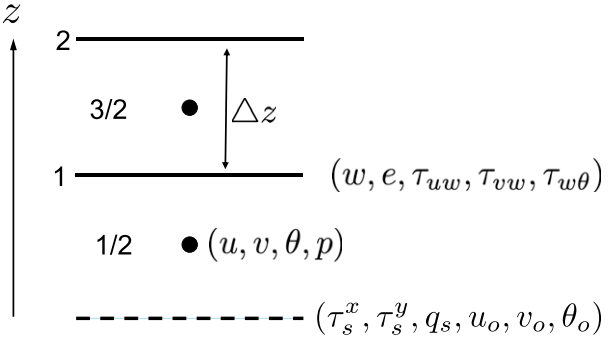

FIG. 5. Sketch of the staggered vertical grid near the water surface used in LES showing the location of field variables discussed in section 4. Surface currents and sea surface temperature (u_o, v_o, θ_o) and surface momentum and temperature fluxes $(\tau_s^x, \tau_s^y, q_s)$ are located at the w level $z = 0$ indicated by the dashed horizontal line. Variables (u, v, θ, p) are located at cell centers (1/2, 3/2), while variables $(w, e, \tau_{uw}, \tau_{vw}, \tau_{w\theta})$ are located at cell faces (1, 2).

the water surface (e.g., Businger 1972). Variables $(u, v, \theta)_{1/2}$ stored at the $z_{1/2}$-level and variables $(u, v, \theta)_o$ stored at the water surface are both used in the M–O formulas. The imposed roughness is $z_o = 2 \times 10^{-4}$ m characteristic of a low or moderate wind marine boundary layer (e.g., Large and Pond 1981). The M–O formulas for friction velocity u_* and temperature flux q_* are coupled because of mutual dependence on the stability parameter $z_{1/2}/L$ where the M–O length $L = -u_*^3/\beta\kappa q_*$ with von Kármán constant $\kappa = 0.4$. Given $(u, v, \theta, z)_{1/2}$ and z_o, a robust bisection iteration scheme solves for (u_*, q_*) in the presence of currents (u_o, v_o) and imposed SST θ_o.

The M–O equations can be interpreted as bulk aerodynamic formulas for momentum and temperature fluxes:

$$\boldsymbol{\tau}_s \equiv (\tau_s^x, \tau_s^y) = -\rho_a C_d |\Delta \mathbf{u}^h| \Delta \mathbf{u}^h, \tag{20a}$$

$$q_s = -\rho_a C_h |\Delta \mathbf{u}^h| \Delta\theta. \tag{20b}$$

The negative sign in (20) is used to indicate surface fluxes are downgradient as in the SGS parameterization. Also in the LES kinematic fluxes $(\boldsymbol{\tau}_s, q_s)/\rho_a$ are used, for clarity density is omitted in Fig. 5 and in Eqs. (22) and (23). The velocity and temperature differences between the $z_{1/2}$-level and the water surface are $\triangle \mathbf{u}^h = \mathbf{u}^h_{1/2} - \mathbf{u}^h_o$ and $\Delta\theta = \theta_{1/2} - \theta_o$. The horizontal momentum flux vector $\boldsymbol{\tau}_s = (\tau_s^x, \tau_s^y)$ is assumed to be aligned with the vector $\Delta\mathbf{u}$, and the average $|\langle \boldsymbol{\tau}_s \rangle|/\rho_a = u_*^2$. The exchange coefficients for momentum and temperature fluxes (C_d, C_h) are found in the bisection iteration scheme, additional details about the scheme can be found in the appendix of Sullivan et al. (2014). We emphasize that Eqs. (20a) and (20b) are coupled and nonlinear rules for surface fluxes. Although we primarily impose SST as the surface boundary condition, we also consider a boundary condition with imposed surface temperature flux. The boundary condition for w is the usual no-flow condition $w = 0$ at $z = 0$. The M–O formulas are applied at every x–y grid point in the LES.

In our discussion it is illuminating to examine the flux deviations from the background far-field average state, i.e., the surface flux anomalies. The normalized anomalies are simply computed from

$$\tau_a(x,y) = \frac{|\langle \boldsymbol{\tau}_s(x,y) \rangle|}{u_*^2} - 1, \quad q_a(x,y) = \frac{\langle q_s(x,y) \rangle}{q_*} - 1, \tag{21}$$

where (u_*, q_*) are far-field values, and angle brackets $\langle\ \rangle$ denote a time average.

c. *Currents and turbulent motions in the boundary layer interior*

To illustrate how the eddy impacted surface fluxes are projected into the boundary layer interior consider the semidiscrete LES equations written at the $(z_{1/2}, z_1)$-levels in Fig. 5:

$$\frac{\partial u_{1/2}}{\partial t} = -\frac{\partial p_{1/2}}{\partial x} - \frac{(uw + \tau_{uw})_1 - \tau_s^x}{\Delta z} + \ldots, \tag{22a}$$

$$\frac{\partial v_{1/2}}{\partial t} = -\frac{\partial p_{1/2}}{\partial y} - \frac{(vw + \tau_{vw})_1 - \tau_s^y}{\Delta z} + \ldots, \tag{22b}$$

$$\frac{\partial w_1}{\partial t} = -\frac{p_{3/2} - p_{1/2}}{z} - \frac{\partial (uw + \tau_{uw})_1}{\partial x} - \frac{\partial (vw + \tau_{vw})_1}{\partial y} + \ldots, \tag{22c}$$

$$\frac{\partial \theta_{1/2}}{\partial t} = -\frac{(w\theta + \tau_{w\theta})_1 - q_s}{z} + \ldots. \tag{22d}$$

The ellipses in (22) denote all other terms in the LES equations that do not depend on the surface fluxes. Notice surface fluxes $(\tau_s^x, \tau_s^y, q_s)$ appear in the vertical gradients on the right-hand side of (22a), (22b), and (22d), and thus explicitly impact the evolution of the (u, v, θ) fields. The pressure $p_{1/2}$, and thus the horizontal and vertical pressure gradients, further depend on the surface fluxes as shown below.

Our Runge–Kutta time-stepping method finds a pressure $p(\mathbf{x})$ at each substep that satisfies the divergence free condition. To expose the role of the surface boundary conditions consider the Poisson pressure equation and its source term near the water surface in Fig. 5. At the $(z_{1/2}, z_{3/2})$-levels the pressure satisfies the semidiscrete equation:

$$\begin{aligned} \Delta t \left(\frac{\partial^2 p_{1/2}}{\partial x^2} + \frac{\partial^2 p_{1/2}}{\partial y^2} + \frac{p_{3/2} - p_{1/2}}{\triangle z^2} \right) &= -\frac{\partial}{\partial x} \left[\frac{(uw + \tau_{uw})_1 - \tau_s^x}{\Delta z} \right] \\ &- \frac{\partial}{\partial y} \left[\frac{(vw + \tau_{vw})_1 - \tau_s^y}{\Delta z} \right] - \frac{1}{\Delta z} \left[\frac{\partial (uw + \tau_{uw})_1}{\partial x} + \frac{\partial (vw + \tau_{vw})_1}{\partial y} \right] \\ &+ \frac{\beta(\theta_1 - \theta_r)}{\Delta z} + \ldots. \end{aligned} \tag{23}$$

where again the ellipses denote all the other source terms on the right-hand side; we have also used the no-flow normal boundary condition $w(z = 0) = 0$, for further details see Sullivan et al. (2014). Inspection of (23) shows the source term in the pressure stencil depends on the horizontal gradients of the surface stress $(\partial_x \tau_s^x, \partial_y \tau_s^y)$ and the temperature at the z_1 grid level where $\theta_1 = (\theta_{3/2} + \theta_{1/2})/2$; because of (22d) temperature flux q_s is implicit in θ_1 and hence $p_{1/2}$. The eddy current $\mathbf{u}_o$ and SST θ_o thus impact the pressure because of surface fluxes (20). Pressure gradients then transfer the current impact to the dynamical fields (u, v, w) in the interior of the boundary layer.

What are the impacts of specifying surface SST versus surface flux in (20b)? If we specify SST then q_s inherits all the variability in the surface winds and temperature, and the underlying eddy current, i.e., $\Delta(\mathbf{u},\theta)_{1/2}$. Variability in the temperature flux directly impacts $\theta_{1/2}$ according to (22d), and hence the pressure. Specifying constant surface temperature flux, however, short circuits variability in the temperature field. There are fluctuations in the exchange coefficients (C_d, C_h) since we use M–O similarity theory to diagnose them, but C_h and $\Delta\mathbf{u}$ variability is balanced by changes in θ_o in (20b), and θ_o does not appear in (22d). Boundary conditions constant θ_o and constant q_s thus produce different levels of variability in $\theta_{1/2}$, the pressure field, and hence the boundary layer. With imposed SST, both wind and temperature fluctuations $(\Delta\mathbf{u}, \Delta\theta)$ result in heterogeneous q_s. Broadly, incorporating oceanic currents in the LES introduces both mechanical and thermal couplings within the overlying atmospheric boundary layer.

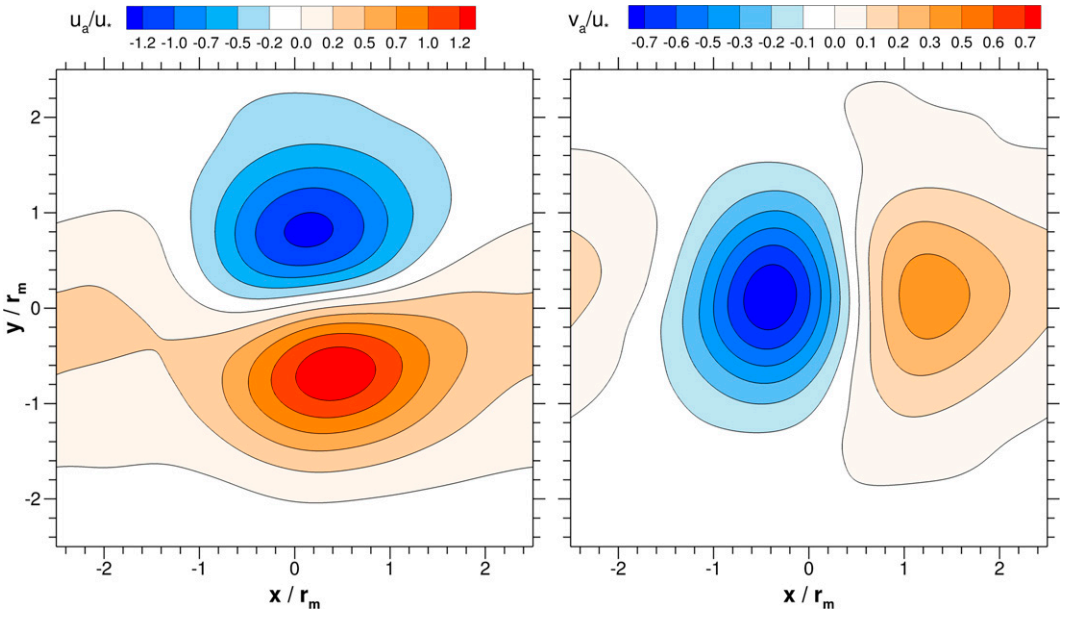

FIG. 6. Variation of horizontal wind anomalies (left) u_a/u_* and (right) v_a/u_* at $z = 7.5$ m from simulation k03 with $u_g = 5$ m s^{-1} and $r_m = 4$ km.

5. Results: Neutral winds

We first examine the impact of winds and currents on boundary layer dynamics under neutral surface conditions, i.e., where $-z/L \to 0$. In contrast to the simulations in sections 6 and 7, these LES experiments impose a temperature flux boundary condition $q_s(x, y) = 0$. This boundary condition isolates the coupling between surface momentum and temperature fluxes in the presence of eddy currents, and also allows a comparison with the linearized Ekman model discussed previously. In simulation k03 the geostrophic wind $u_g = 5$ m s^{-1}, the eddy radius $r_m = 4$ km, and $\epsilon = 0.466$. The LES domain size, number of mesh points, and bulk parameters are provided in Table 1. Note the smaller values of friction velocity u_* and boundary layer depth z_i in the absence of convective forcing. Thus the ratio z_i/r_m is smaller than in the mixed shear-convective cases in section 7.

A robust feature of all simulations is the development of organized variability in the surface momentum flux, a flux dipole shown in Fig. 1 which is also predicted by the Ekman model. To compare with (14), we process the LES output and compute the average stress anomaly (21); to further smooth the results, a low-pass filter is applied with filter $\delta = 2$ km. The theory-simulation comparison in Fig. 1 shows good qualitative and quantitative agreement. The peak magnitude of the stress anomaly occurs near $x = 0$ and $y/r_m \sim \pm 0.707$, i.e., where U_s is maximum. Simulation k01 with $u_g = 2.5$ m s^{-1} and $\varepsilon = 0.932$ with smaller values of u_* and z_i generates a similar flux dipole as in Fig. 1 with (positive, negative) perturbations over the (north, south) quadrants of the eddy. Anticyclonic eddies $\varepsilon < 0$ in the LES and also in the Ekman theory reverse the sign of the anomaly. At $z = 7.5$ m, the near surface horizontal velocity anomalies $(u_a, v_a)/u_* \sim O(1)$ are well correlated with the surface momentum flux but are noticeably shifted to the north and east of the eddy center as shown in Fig. 6; the horizontal vector $\mathbf{u}_a$ exhibits a cyclonic swirling motion about the location $(x, y)/r_m = (0.6, 0.2)$ at $z = 7.5$ m and at $(x, y)/r_m = (1.4, 0.5)$ at $z = 59$ m, see supplementary material. With increasing height, advection continues to shift the horizontal and vertical anomaly patterns further to the northeast, and at the same time the magnitude of the anomaly decays. For $z > 59$ m the coherent signature of the eddy disappears in the background turbulence and the horizontal motions morph into a streamwise oriented pattern.

A demanding test compares the vertical velocity w from the Ekman model and the LES. One qualitative difference is that the unstratified Ekman model has $w \to w_e$ as z increases, and it extends to an arbitrary height. In contrast in the stratified LES w does not penetrate beyond the inversion layer, partly because of the $w = 0$ boundary condition at the top of the LES domain; therefore, we compare its w field at an intermediate level within the ABL. Figure 3 depicts the pumping velocity w_e from (15) with the vertical velocity anomaly computed from simulation k03 at $z = 60.5$ m. The fields in Fig. 3 are each normalized by $(u_*^2\varepsilon)/(fr_m)$ suggested by (15). The comparison is interesting. At $z = 60.5$ m ($z/z_i = 0.19$), the LES predicts the center of the downdraft is offset to the northeast and is surrounded by weaker updrafts in qualitative agreement with the Ekman model. However, the magnitude of the updraft and downdrafts is considerably weaker in LES. Tracking the vertical path of the downdraft–updraft pattern in the LES shows it is offset from the eddy center at all z with maximum positive and negative magnitudes near $z/z_i = 0.19$. Vertical cutting planes x–z at $y/r_m = 0.7$ and y–z at $x/r_m = 0.8$ show the vertical organization of w induced by the eddy is confined to the near surface. For case k01 with $\varepsilon = 0.933$ the

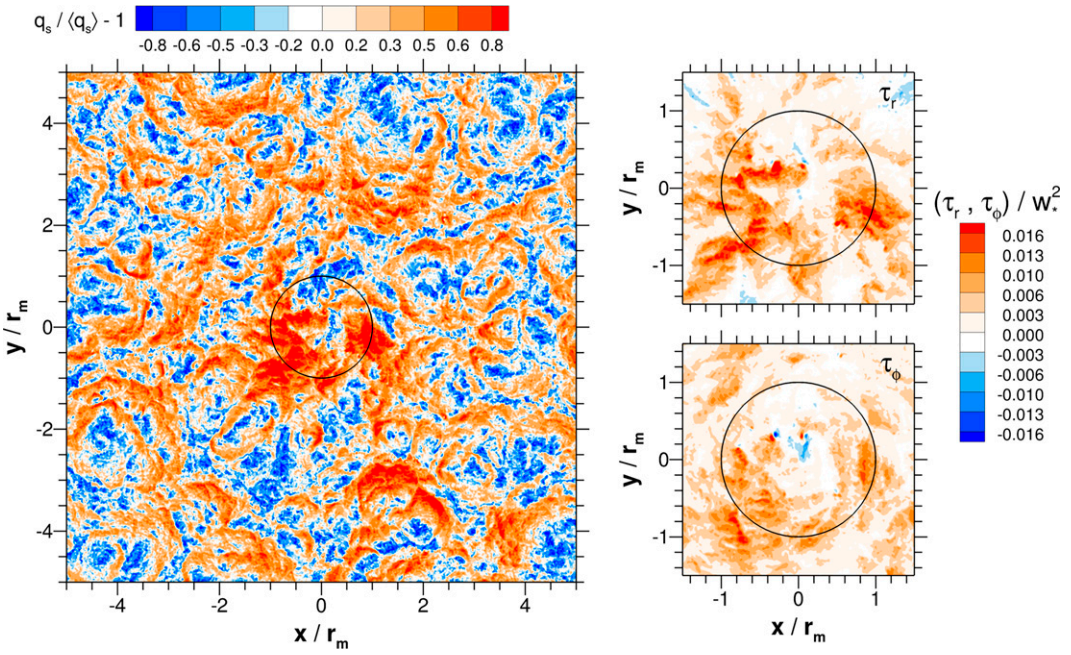

FIG. 7. Variation of surface fluxes in free convection coupled to a cyclonic oceanic eddy with $r_m = 400$ m. (left) Surface temperature flux q_s normalized by $\langle q_s \rangle$ and (right) a zoom of the (radial, azimuthal) momentum fluxes (τ_r, τ_ϕ) normalized by w_*^2. The black circle has radius $r/r_m = 1$. Results from simulation f08 with 10-times-larger eddy radius $r_m = 4$ km are shown in the supplementary material.

magnitude of the vertical velocity anomaly increases by more than a factor of 2 compared to case k03 with $\varepsilon = 0.466$; and the pattern of downdrafts and updrafts is more coherent over the depth of the ABL. Changing the sign of eddy rotation in simulation k04 simply reversed the updraft and downdraft patterns compared to k03 but otherwise did not alter the magnitude of the vertical velocity.

The results from simulations k03 and k04 motivated further investigation. An Ekman simulation m01 with $u_g = 5$ m s^{-1} and $r_m = 4$ km was carried out to remove stable stratification impacts on the eddy induced motions: Recall k01, k03 and k04 are stably stratified at all z but especially at z levels near the ABL inversion. The LES Ekman simulation m01 develops vigorous turbulence over the depth of the ABL $z_i \sim 700$ m but we readily identify the same eddy induced flux dipole and vertical velocity anomaly as in Figs. 2 and 3. Inspection of the LES Ekman solution also shows a complex transition from the downdraft–updraft pattern near the surface to an elongated streamwise pattern for $z > 100$ m. The amplitude of the horizontal motions at $z > 100$ m are large, nearly a factor of 5 greater than the eddy induced vertical velocity. Horizontal advection that varies with z appears to be the main source of disagreement between the linearized Ekman model and the LES, not stratification influences.

6. Results: Free convection

Idealized free convection, no mean wind (e.g., Schmidt and Schumann 1989), is the asymptotic stability regime $-z/L \to \infty$ frequently used to examine the impact of land surface heterogeneity on the atmospheric boundary layer (e.g., Raasch and Harbusch 2001; Owinoh et al. 2005; Patton et al. 2005). Flow visualization and analysis of our LES runs also shows unique features in the free convection regime when coupled to an oceanic eddy with heterogeneous currents.

As discussed in sections 4b and 4c even with fixed SST, the surface temperature flux depends on the eddy currents and overlying turbulent winds because of coupling in the surface flux formulas (20). A cyclonic eddy with radius $r_m = 400$ m interacting with convective turbulence generates rich variability in the surface flux as shown in the left panel of Fig. 7. Close inspection shows a high concentration of positive temperature flux at $(x, y) = (0, 0)$, the instantaneous flux at the eddy center frequently exceeds 60% of the average flux $\langle q_s \rangle$. In regions outside of the eddy the flux is often less than 50% of $\langle q_s \rangle$. Coupling the currents with the overlying winds also results in spatially intermittent momentum flux. The right panel of Fig. 7 shows the distribution of radial and azimuthal momentum fluxes (τ_r, τ_ϕ) near the eddy center. Notice (τ_r, τ_ϕ), computed from (τ_s^x, τ_s^y), although intermittent are biased toward positive values near the eddy center because of the surface wind directions, see discussion below.

Eddy currents coupled to surface fluxes in free convection leave an imprint on the full atmospheric boundary layer particularly in the pressure and temperature fields and to a lesser degree the vertical velocity field, see Figs. 8 and 9. The (p, θ) fields show horizontal organization at a scale larger the boundary layer depth z_i and eddy radius r_m. Based on the decay of the eddy current in (19), $U_s/U_{s,m} \approx 0.06$ at $r/r_m = 2.1$ and thus we expect to observe an impact on θ and p at scales with an upper bound $r \sim 1$ km. At the water surface, the

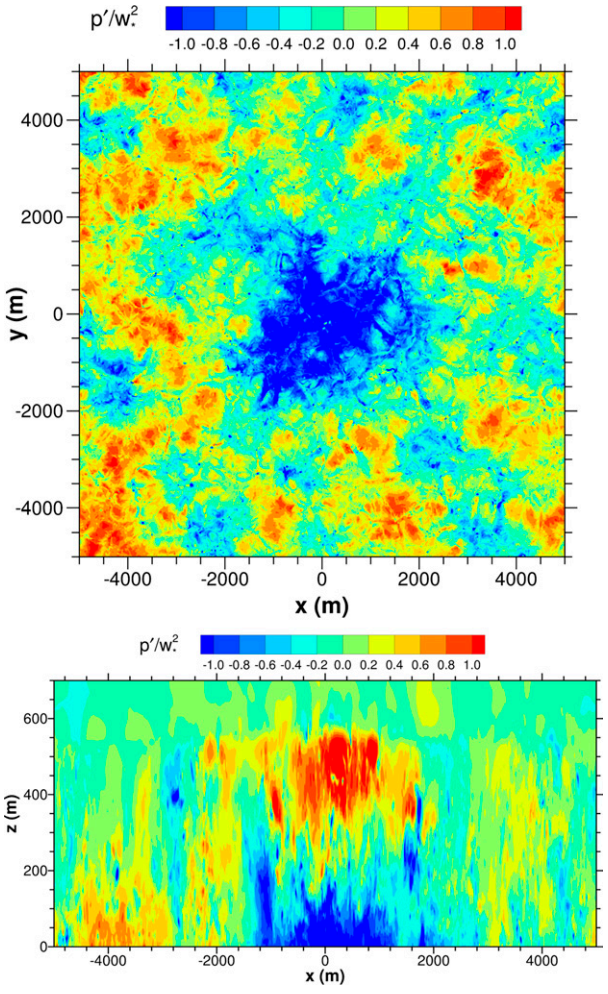

FIG. 8. Fluctuating pressure $p' = p - \langle p \rangle$ normalized by w_*^2 (top) in an x–y plane near the surface $z = 7.5$ m and (bottom) in an x–z plane at $y = 0$ m from simulation f01.

coherent negative pressure at the eddy center is nearly 1 km wide and is surrounded by an outer ring of less organized positive pressure. The coupling between large horizontal scales in p and θ at the surface is contained in (23). We find that the LES requires a horizontal domain of 10 km in order to resolve the pressure field organization; coherent pressure first begins to develop midway through the simulation. An x–z plane cutting through the eddy center, see the bottom panel of Fig. 8, shows that the pressure organization extends over the full depth of the boundary layer, a sign change (positive pressure) occurs in the middle and upper boundary layer.

At the surface the θ field exhibits two scales, a wide slightly warm core overlain with a web of warmer narrow intersecting filaments; the former is induced by the oceanic eddy while the latter is a characteristic convection feature found over a homogeneous surface (e.g., Schmidt and Schumann 1989; Sullivan and Patton 2011). Near the boundary layer top a strong and wide central updraft, induced by a secondary circulation, is surrounded by clusters of smaller plumes arranged in a ring of radius ~ 2 km. The no flow boundary condition on vertical velocity prevents w from developing the larger horizontal scale observed in the θ field near the surface. Depending on the horizontal position of an x–z or y–z cutting plane we also observe intense splats in u or v at the ABL inversion. Similar results are obtained for cyclonic and anticyclonic eddies, i.e., changing the sign of the eddy rotation does not change the sign of the (p, θ) fields. Apparently oceanic eddies can act as an agent to organize structures over the depth of the boundary layer in free convection.

It is interesting to contrast our convective boundary layer results with analytic models of neutral rotating boundary layers (e.g., Schlichting 1968; Rotunno 2013, 2014). To facilitate the comparison the LES surface fluxes (τ_s^x, τ_s^y) and horizontal velocities (u, v) are first converted into radial and azimuthal components $(\tau_r, \tau_\phi, v_r, v_\phi)$ at each (x, y) location. These variables and w are then interpolated to a fine polar (r, ϕ) mesh, and integrated around a ring $\phi = [0, 2\pi]$ at fixed values of r. Finally, these results are averaged in time; square brackets [ ] in the narrative below indicate a time average in (r, ϕ) polar coordinates.

Results for the surface fluxes $[\tau_r, \tau_\phi, q_s]$ are shown in Fig. 10 for cyclonic and anticyclonic eddies. Notice the temperature and momentum fluxes peak near $r = 0.7\ r_m$ where the eddy current is maximum. Fluxes $[\tau_\phi, q_s]$ decay with increasing $r > r_m$. Noteworthy is that the flux τ_r tends to u_*^2 at large r, thus the radial flow near the surface is inward toward the low pressure region in Fig. 8. The spatial variation of the fluxes is similar for cyclonic and anticyclonic eddies, but with a sign change in τ_ϕ, the sign of τ_ϕ matches the eddy rotation. The magnitude of the temperature flux at $r/r_m = 1$ depends on the eddy rotation; $[q_s]$ is noticeably larger for the anticyclonic case compared to its cyclonic counterpart. Recall the linear Ekman model [Eq. (15), section 2] predicts a central updraft for anticyclonic rotation. In the LES there is cooperative behavior between surface convection and anticyclonic eddy rotation that enhances the surface temperature flux.

Average velocity fields $[v_r, v_\phi, w](r, z)$ are shown in Fig. 11 at four different vertical levels $z = (7.5, 184.0, 409.0, 646.0)$ m for simulations with cyclonic and anticyclonic eddies. Inspection of the results shows that the oceanic eddy has generated a large scale coherent SC under free convection. The radial flow $v_r < 0$ is inward toward the eddy center over the bulk of the boundary layer $r/r_m = [0, 12]$ and $z/z_i < 0.5$. Vertical velocity $[w] > 0$ is concentrated in an updraft near the eddy center, the strength of the updraft increases with vertical distance from the surface as expected. In the middle of the boundary layer, $[w] > (v_r, v_\phi)$ as a result of the potent SC. In the inversion layer the updraft w is quenched and the resulting splat induces outward radial motion $v_r > 0$. The sign of the azimuthal velocity v_ϕ in the lower boundary layer depends on the direction of the eddy rotation. The surface stress τ_ϕ acts to *drag* the surface winds in the same direction as the eddy rotation, i.e., similar to a plane Couette flow. In the middle and upper boundary layer v_ϕ is weak but greater than zero. In the anticyclonic case v_ϕ switches sign near $z_i/2$, and we speculate the sign switch is a consequence of positive Coriolis rotation. The sign of the central updraft is independent of the sign of the

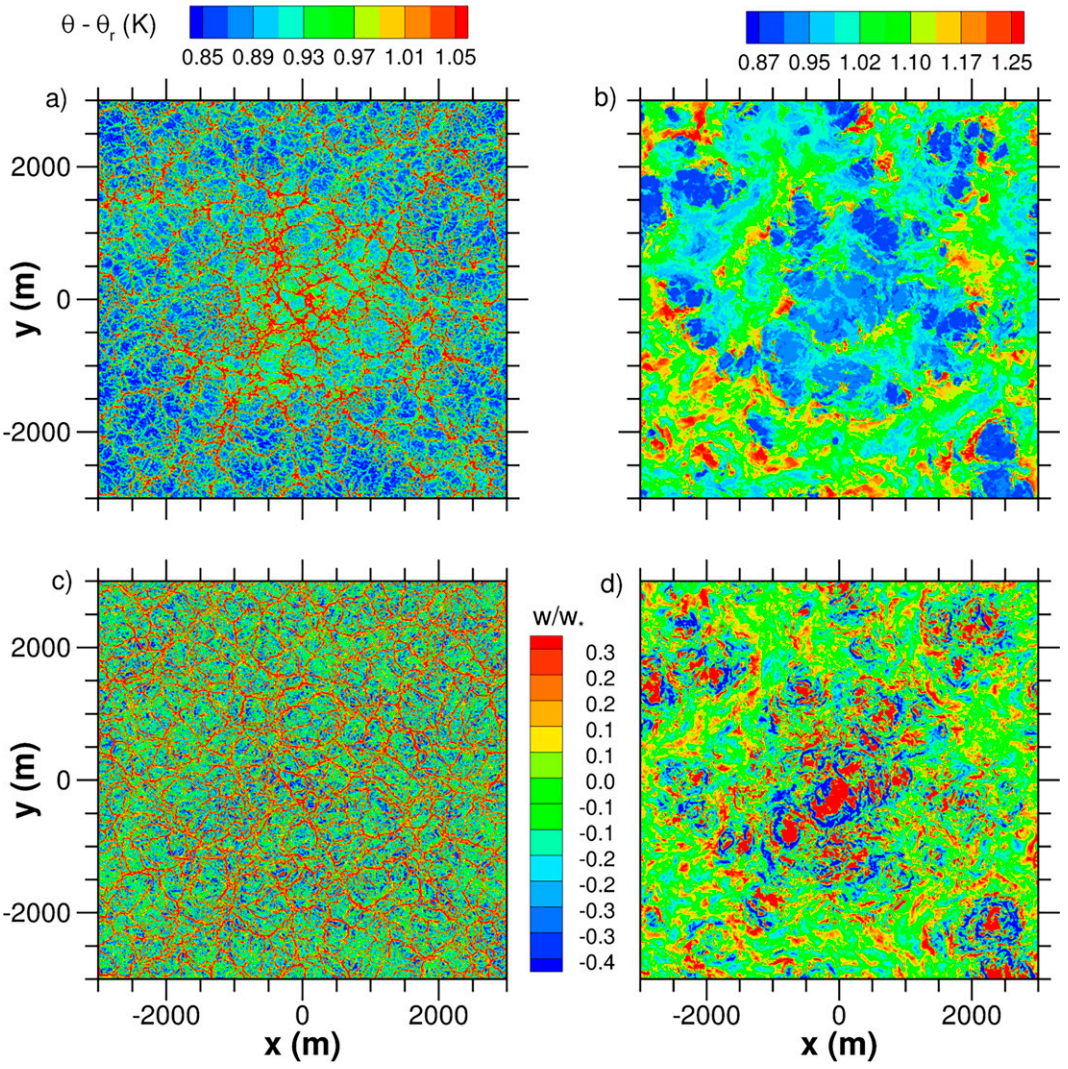

FIG. 9. Temperature $\theta - \theta_r$ in an x–y plane (a) near the water surface $z = 7.5$ m and (b) near the boundary layer top $z = 524$ m. Vertical velocity w/w_* at (c) $z = 7.5$ m and (d) at $z = 524$ m. Results are from simulation f01 and only a fraction of the horizontal domain is shown.

rotation, i.e., $[w] > 0$ independent of the rotation, markedly different than the neutral regime in section 5. However, in the interior of the ABL, vertical velocity $[w]$ for $0 < r/r_m < 1.5$ is noticeably enhanced with anticyclonic eddy rotation. As mentioned previously, this is a signature of cooperative behavior between surface convection and the central updraft induced by the eddy rotation.

Thus a circular eddy of modest strength generates a SC in the free-convective atmospheric boundary layer that draws in fluid at the bottom and expels fluid vertically upward into the interior of the boundary layer. Near the top of the boundary layer the rising plume splashes against the stably stratified inversion and the splat generates a radial outflow. The outflow is deflected downward and the descending shell away from the eddy center feeds the radially inward flow at the surface completing the circulation. Thus the surface eddy and convection act in concert to create a secondary circulation. In a neutral cyclonic rotating boundary layer discussed in section 2 and by Schlichting (1968), Rotunno (2013, 2014) the SC features a downdraft at the center with outward radial flow near the surface. Convective boundary layer turbulence coupled to an oceanic eddy produces a SC that is opposite in sign and different compared to a neutral rotating boundary layer. The results depend on the sign of the eddy rotation and the surface boundary condition for temperature.

In a two-step process, eddy currents first generate spatial heterogeneity in the surface temperature flux with fixed SST. Then the resulting heterogeneity in $q_s(x, y)$ acts to drive organized depth-filling secondary circulations similar to atmospheric flows with heterogeneous SST fronts as shown in S20 and S21. A surface boundary condition that holds q_s spatially constant eliminates surface heterogeneity and SC even in the

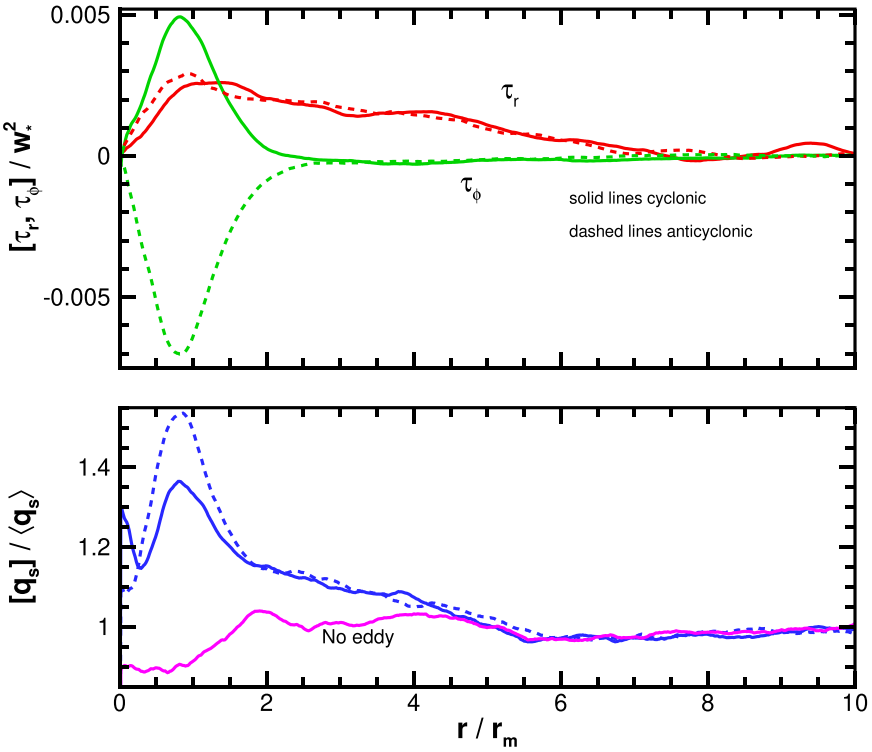

FIG. 10. Average radial and (top) azimuthal surface momentum fluxes (τ_r, τ_ϕ) and (bottom) surface temperature flux (q_s). Simulations of free convection above a cyclonic (solid lines) and anticyclonic (dashed lines) eddy with r_m = 400 m. For reference, surface temperature flux for no eddy, case f04, is indicated by the pink solid line in the bottom panel.

presence of currents. To test these ideas simulation f05 imposes a flux boundary condition with no currents, but uses a point-by-point time average flux $\overline{q_s(x,y)}^t$ built from simulation f01, see supplementary material. The spatial organization in the (p, θ, w) fields from f05 match those obtained from f01 (not shown). In other words, spatial heterogeneity in $q_s(x, y)$ generated by coupling eddy currents in the surface flux formulas is responsible for the observed organization in free convection. Simulation f08 with a 10-times-larger radius r_m = 4 km generates a similar impact on the ABL as r_m = 0.4 km; see supplementary material.

7. Results: Winds and convection

To examine the combined impact of winds, convection, and currents on boundary layer dynamics in an intermediate regime of $-z/L$ a suite of LES experiments are carried out varying the geostrophic wind u_g = (2.5, 5) m s^{-1} and eddy radius r_m = (0.4, 1.2, 2, 4) km. In these simulations the SST is adjusted to generate an average temperature flux q_s similar to that in the free convection experiments. The LES details and bulk parameters are provided in Table 1. We focus on simulations with r_m = 4 km, but touch on the impact of smaller r_m. For discussion purposes it is convenient to divide the circular eddy into four quadrants (left, upper, right, lower) referred to as (west, north, east, south) quadrants, respectively.

a. Surface flux anomalies

In the intermediate regime of $-z/L$ an oceanic eddy generates flux anomalies that differ from the coherent structures in a homogeneous flow, and are also different than the anomalies in the free convection and neutral regimes discussed previously. Typical results for (τ_a, q_a) from cases i04 (no eddy) and i03 (with an eddy) are compared in Fig. 12. In both simulations the winds are light u_g = 2.5 m s^{-1} and the average fluxes (u_*, q_*) ~ (0.096 m s^{-1}, 0.013 K m s^{-1}). Because of Coriolis rotation the surface winds are weakly rotated from the x axis. In i03 the eddy rotation is cyclonic, r_m = 2 km, and the ratio of the boundary layer depth to eddy radius z_i/r_m = 0.35. To emphasize the impact of the oceanic eddy on the magnitude and scale content of the anomalies, the average fluxes computed from (21), shown in Fig. 12, are further low-pass filtered using a Gaussian filter with scale δ = 500 m.

In the horizontally homogeneous case i04 (no eddy), the momentum and temperature flux perturbations are streaky anisotropic structures mainly aligned with the streamwise wind at all scales. ABL turbulence generates flux fluctuations mainly at scales less than 500 m; (τ_a, q_a) are less than 10% of (u_*^2, q_*) at scales greater than 500 m. In the heterogeneous case i03 (with an eddy), the anomaly patterns are spatially organized, coherent in time, and are concentrated at scales larger than 500 m. The stress anomaly is (more, less) negative in the (north, south) quadrants, respectively, similar to the

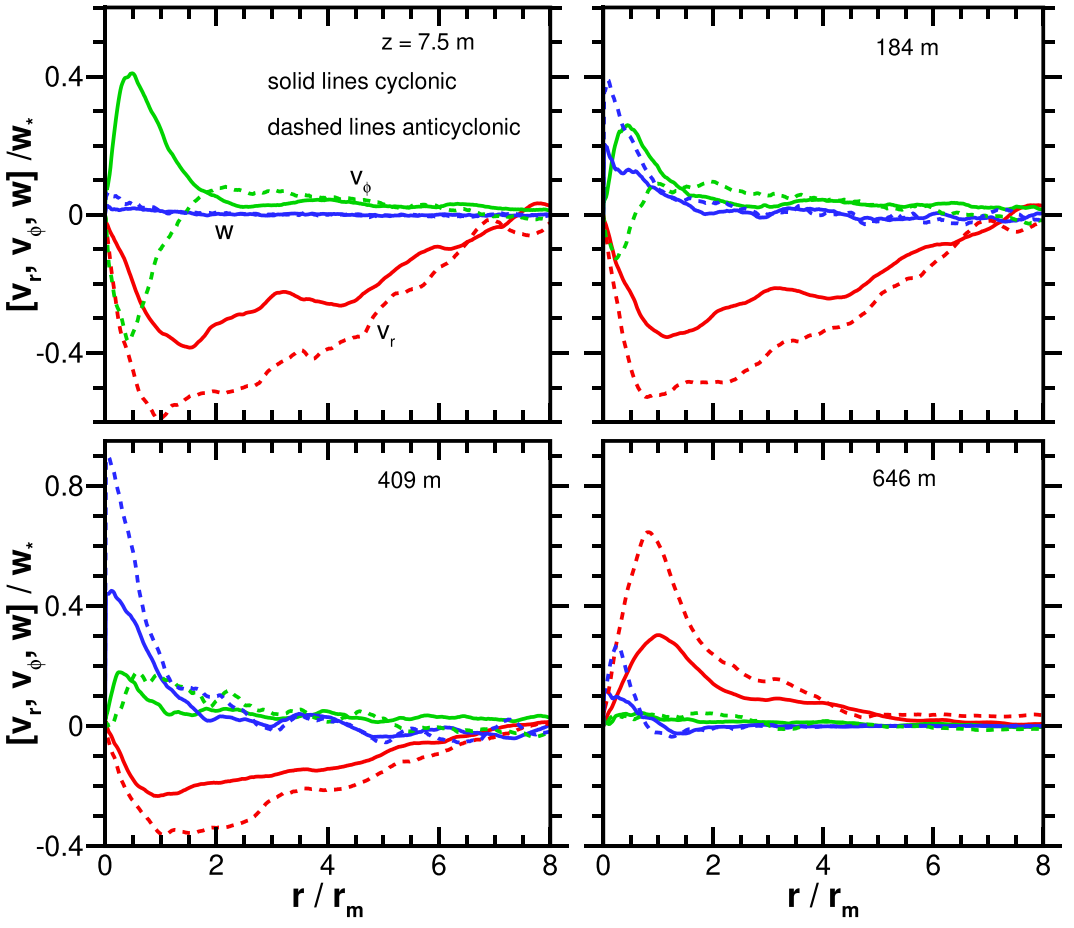

FIG. 11. Average radial v_r, azimuthal v_ϕ, and vertical w velocities (red, green, blue colors, respectively) for simulations of free convection above a cyclonic (solid lines) and anticyclonic (dashed lines) eddy. The vertical levels are $z = (7.5, 184.0, 409.0, 646.0)$ m and $r_m = 400$ m.

neutral regime. In all simulations with an eddy, coherent momentum fluxes are observed with horizontal scales dependent on the eddy radius r_m.

The momentum flux organization is explained by the wind and current alignment. Given $u_{1/2} > 0$, in the north quadrant $u_o < 0$ and then τ_s^x is large while in the south quadrant $u_o > 0$ and then τ_s^x tends to zero. The spanwise momentum flux τ_s^y also develops a dipole because of wind–current coupling $\Delta v = v_{1/2} - v_o$. Under positive Coriolis rotation $v_{1/2} > 0$, Δv is positive and large in the west quadrant and small or negative in the east quadrant.

The new feature in the mixed shear-convection regime is the formation of a temperature flux dipole. Even with spatially uniform $\theta_o(x, y)$ a temperature flux dipole develops because of wind–current coupling $|\triangle \mathbf{u}|$ in (20b). Under unstable conditions $\Delta\theta < 0$, q_s in the (north, south) quadrant is (larger, smaller), respectively. In the south quadrant wind–current coupling nearly switches the temperature flux to stable forcing, i.e., locally the M–O stability parameter $-z/L$ is very unstable in the north quadrant while in the south quadrant $-z/L$ tends to neutral. The eddy radius r_m plays an important role in the dipole pattern as the latter is enhanced with larger r_m, i.e., as r_m/z_i increases the impact of the heterogeneous currents also increases. The sign and spatial dipole patterns in the bottom panels of Fig. 12 reverse with an anticyclonic eddy (not shown). Thus oceanic eddy currents can modify both momentum and temperature fluxes in an intermediate regime of $-z/L$. The surface fluxes are (largest, smallest) where winds and currents are (opposed, aligned). For the low wind case i03, the normalized peak (stress, temperature flux) anomalies are approximately (0.7, 0.3) or about (0.0074 N m^{-2}, 4.8 W m^{-2}), respectively.

All simulations with an eddy generate flux patterns qualitatively similar to those shown in the bottom panels of Fig. 12. To compare the main features of the flux dipoles a spanwise cut through the anomalies at $x = 0$ is collected from each simulation and presented in Fig. 13; the cut at $x = 0$ passes near the maximum and minimum in the dipoles. In each case, the maximum (positive) magnitude occurs near $y = 0.7\ r_m$, i.e., where the eddy current $u_o/U_o < 0$ is a negative maximum (Fig. 4). The magnitude of q_a is consistently smaller by a factor of 3 compared to τ_a. For a fixed eddy radius, the magnitude of τ_a increases with decreasing wind speeds. For example comparing cases (i07, i05) with $r_m = 2$ km the magnitude of τ_a

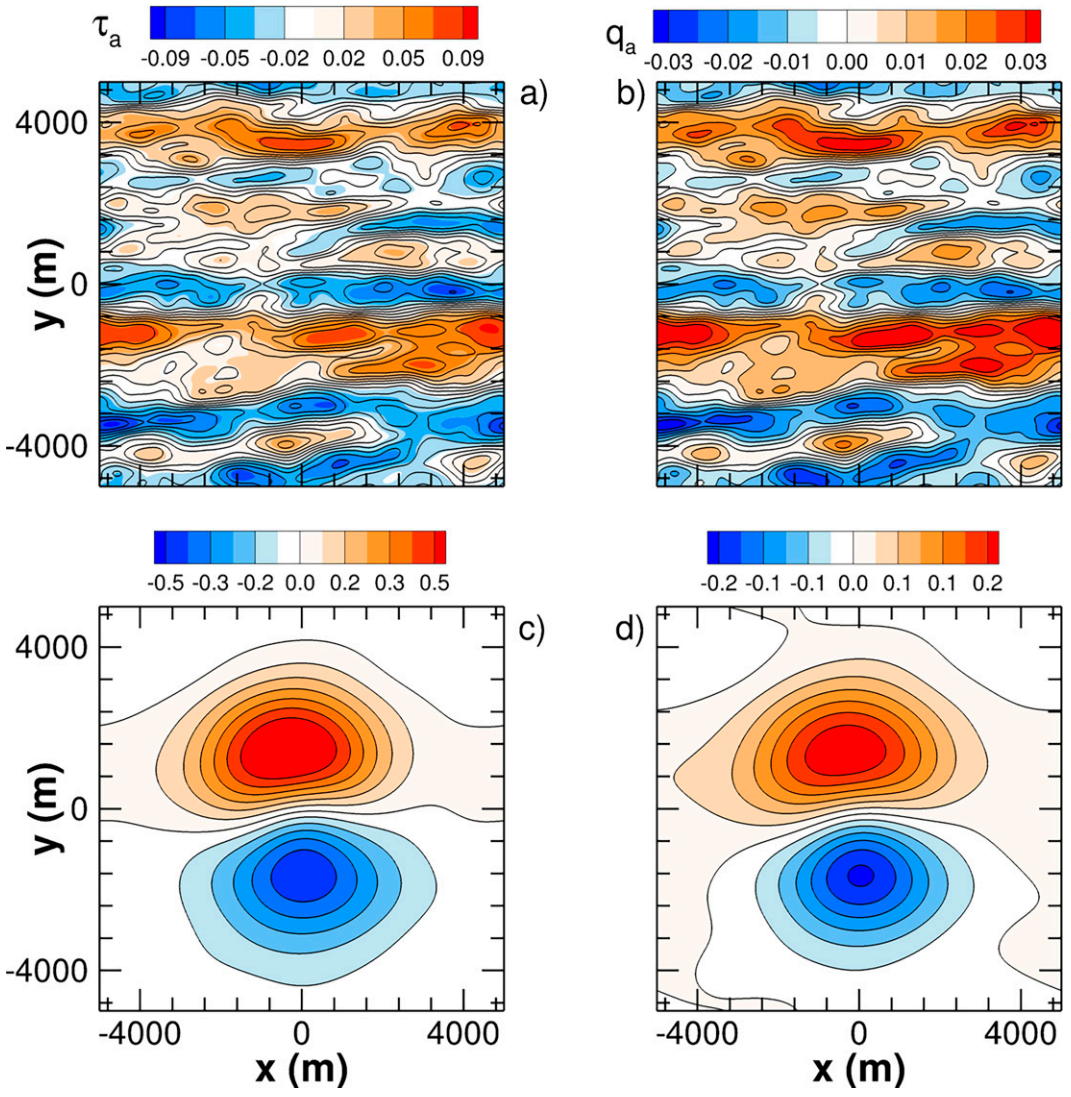

FIG. 12. (a),(c) Surface momentum anomaly τ_a and (b),(d) surface temperature flux anomaly q_a for simulations driven by a mix of shear and convection. (top) Simulation i04 with no eddy and (bottom) simulation i03 with an eddy. The geostrophic wind $u_g = 2.5$ m s^{-1}, $q_* \approx 0.013$ K m s^{-1}, and in i03 $r_m = 2$ km. Results are obtained from a low-pass filter of the flux fields with filter scale $\delta = 500$ m. Note an eddy of 2 km increases the anomaly magnitudes by nearly a factor of 10 at scales larger than δ compared to simulations with no eddy.

increases from 0.4 to 0.8 as u_g decreases from 5 to 2.5 m s^{-1}. This approximate linear dependence is predicted by the linearized Ekman theory, recall the eddy impact varies with $\varepsilon = U_o/u_g$. Convection does not markedly alter the observed patterns, an 83% increase in surface convection in case h04 leads to (normalized) anomalies nearly identical to i07 (not shown). For a fixed wind speed, notice the scale content of (τ_a, q_a) widens with increasing r_m; the LES are mainly in the regime $z_i/r_m \leq 1$. In other words the scale content of the surface flux which the ABL "feels" widens as r_m increases.

It is important to notice that the spanwise gradients $\partial_y(\tau_a, q_a)$ increase with decreasing r_m at fixed wind speed, and thus we anticipate that the impact of current heterogeneity also increases as described in S20 and S21. With eastward u_g, the surface wind is mainly aligned with the x direction but has a small ageostrophic component in the y direction. This combination of surface winds and spanwise gradients in the anomalies is in the "alongfront" regime discussed in S21. With alongfront winds, pressure gradients are equally or more important than mean horizontal advection and the induced secondary circulation is in a plane perpendicular to the alongfront wind direction. However, the sign of the secondary flow in the present simulations depends on the sign of the eddy rotation, see Fig. 13.

b. Boundary layer interior

With mixed shear and convection an oceanic eddy generates organized motions in the turbulent fields near the surface

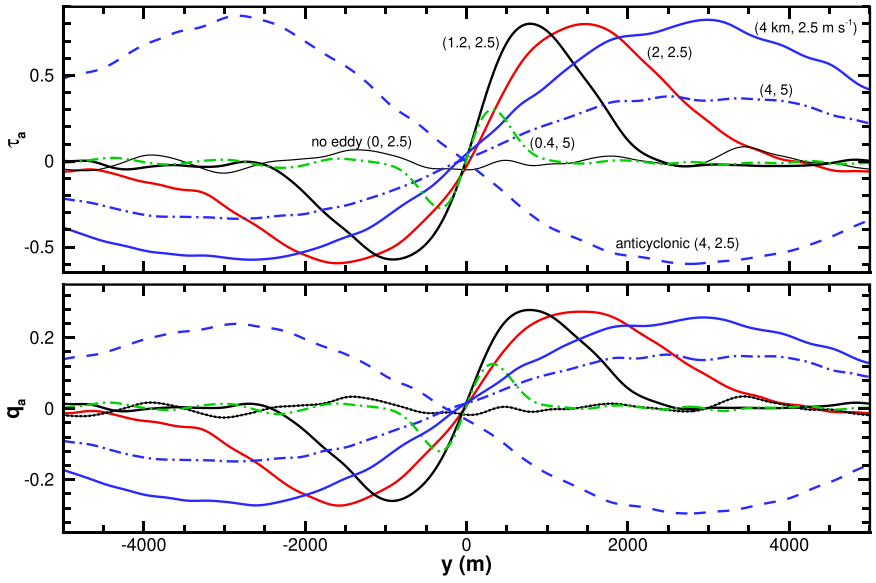

FIG. 13. Variation of (top) surface momentum and (bottom) temperature flux anomalies (τ_a and q_a, respectively). Each curve is labeled with the particular combination of (r_m, u_g) used in the simulation, see Table 1. The results are extracted from 2D contour fields, as shown in Fig. 12, for varying y at $x = 0$. Note the simulation domain with $r_m = 4$ km is 20 km in the horizontal directions.

but also persistent patterns in the interior of the ABL often extending up to the inversion. The eddy imprint in the shear-convection regime is not as dramatic as in free convection but is clearly visible in the temperature field. Eddy induced patterns strengthen with increasing r_m and decreasing wind u_g and are noticeably different than observed in free convection. Visualization in horizontal planes near the surface and ABL inversion shows two scales in θ, an extended streamwise streaky pattern with spanwise width $\approx r_m$. And the streamwise pattern is punctuated with smaller scale updrafts and updrafts associated with boundary layer convection. In the case of a cyclonic eddy, the updrafts and downdrafts are stronger and weaker over the north and south sides of the eddy, see Fig. 12. Very near the surface the (u, v, θ, p) patterns mimic the closed dipoles observed in the surface fluxes, e.g., Fig. 12. With increasing z the eddy induced motions weaken against the background turbulence as the spatial patterns broaden in x and morph into elongated ellipses centered over the surface anomalies. The major axis of the ellipse is aligned with the geostrophic wind, and tends to span the entire x extent of the LES domain.

We use a combination of time and space averaging and low-pass filtering to identify the eddy induced anomalies in the 3D turbulent fields. It is insightful to examine the anomaly directly over the eddy by viewing results projected onto a y–z plane, i.e., in the plane perpendicular to the geostrophic wind. An anomaly for a field h is computed from

$$h_a(y,z) = \overline{h - \langle h \rangle_f}^{xt}, \tag{24}$$

where the overbar operator denotes an average in t and x over the limited interval $[-0.8, 1.5]$ r_m: $\langle h \rangle_f$ is the far-field upstream average. To extract the induced motions a Gaussian filter with scale $\delta = 1$ km is finally applied in the y direction at each z. Results for simulations with $u_g = 2.5$ m s^{-1}, i05 cyclonic eddy $r_m = 4$ km, and i06 anticyclonic eddy $r_m = 4$ km are shown in the four-panel plots in Figs. 14 and 15, respectively. Each figure shows four fields $(v, w, \theta, p)_a$. For easy comparison the figures use the same color bar ranges, and the fields are dimensionless using proper combinations of (w_*, q_*). For a horizontally homogeneous (no eddy) surface vertical velocity anomalies from shear-convection "rolls" (e.g., Moeng and Sullivan 1994; Conzemius and Fedorovich 2006) are equal to zero when averaged over an x–y plane. The impact of an oceanic eddy is clearly visible in Figs. 14 and 15. An eddy with horizontal scale $r_m > z_i$ sets the horizontal scale of persistent anomalies $(v, \theta, p)_a$ that extend over the depth of the ABL; the eddy also appears to provide a mechanism to excite stronger vertical motions in mid-ABL. Notice the anomalies are responsive to the sign of the eddy rotation, for example, near the surface p_a and $\partial_y p_a$ reverse sign for cyclonic and anticyclonic eddies. Closer inspection of the results shows that the pressure gradient $-\partial_y p_a$ drives a (positive, negative) spanwise anomaly v_a near the (surface, inversion), respectively. The pressure field responds to the baroclinic changes in temperature. Notice the underlying eddy motion produces large-scale horizontal variability in θ_a near the inversion which can influence entrainment. As mentioned previously, the orientation of the geostrophic wind relative to the eddy-induced temperature heterogeneity in the present flows is analogous to the "alongfront wind" regime examined in S21. With alongfront winds pressure gradients are of importance in generating organized secondary circulations. The eddy induced motions decrease with $\varepsilon = U_o/u_g$, e.g., the motions are weak in

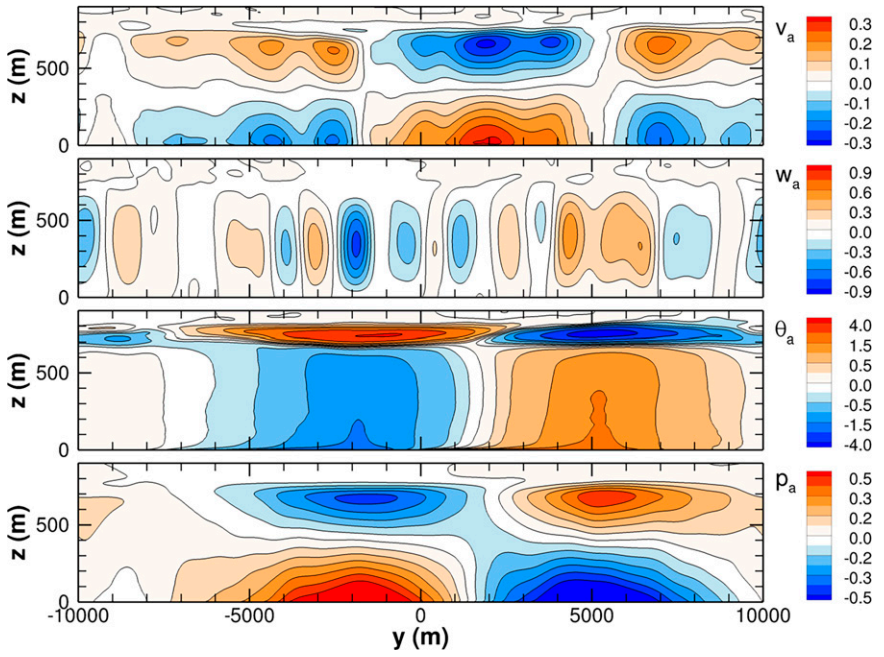

FIG. 14. Average anomaly fields from simulation i05 above a cyclonic eddy $r_m = 4$ km. (from top to bottom) v_a/w_*, $w_a \times 10/w_*$, $\theta_a w_*/q_*$, and p_a/w_*^2, respectively.

simulation i07 with $u_g = 5$ m s^{-1} which is anticipated given the variation of surface fluxes in Fig. 13.

Two-dimensional streamtraces (average particle paths) in a y–z plane at $x/r_m = 4.375$ constructed from anomalies $(v, w)_a$ illustrate the formation of a persistent SC in the interior of the ABL downstream of the eddy center; see supplementary material. The center of the SC is positioned off axis above the north side of the eddy for both cyclonic and anticyclonic

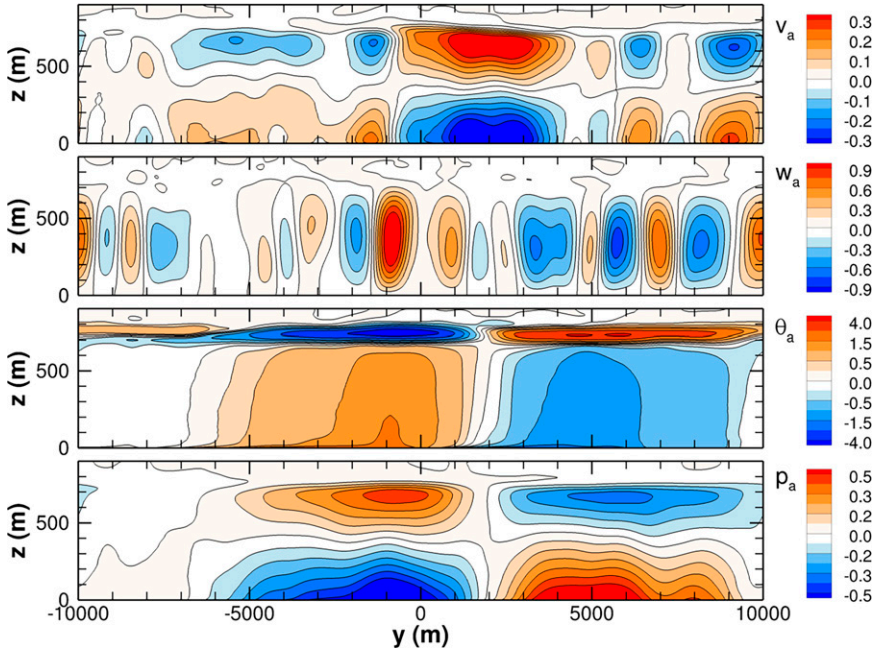

FIG. 15. Average anomaly fields from simulation i06 above an anticyclonic eddy $r_m = 4$ km. (from top to bottom) v_a/w_*, $w_a \cdot 10/w_*$, $\theta_a w_*/q_*$, and p_a/w_*^2, respectively. A comparison with Fig. 14 shows the anomaly fields respond to the sign of the eddy rotation.

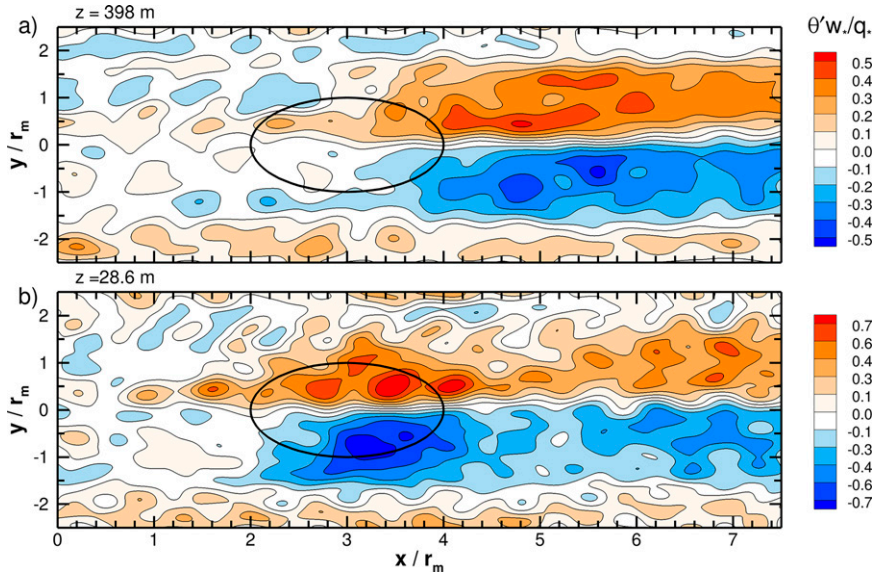

FIG. 16. Average temperature anomaly from simulation i08 above an isolated cyclonic eddy r_m = 2 km, with u_g = 2.5 m s^{-1} at two levels in the ABL: z = (a) 398 and (b) 28.6. The black ellipse marks an eddy radius equal to r_m; the x–y aspect ratio of the plot is not equal to unity.

eddies, and the spanwise extent of the eddy, approximately 4 km, matches the eddy radius r_m. Weaker circulations (not shown) are also present left and right of the dominant SC and are believed to be residuals from limited averaging.

c. *Eddy "wake"*

The vertical coherence of the eddy-induced motions found in section 7b is surprising and motivated additional investigation focusing on their horizontal coherence. Because of the horizontal periodicity in the LES, simulations in Table 1 are essentially flow over a periodic train of eddies. To examine horizontal coherence in the ABL above an isolated (nonperiodic) oceanic eddy we utilize the fringe method introduced in S20 and S21. The fringe technique utilizes small and large LES domains. The turbulent inflow to the large LES domain is nudged to match the homogeneous fields in the small LES domain effectively eliminating periodicity effects, see S20 for details. The forcing conditions are geostrophic wind u_g = 2.5 m s^{-1} with SST set to match simulation i03. In the large LES domain a cyclonic eddy with r_m = 2 km is located $3r_m$ downstream (to the right) of the inflow. The horizontal dimensions of the large domain are (20, 10) km utilizing the spatial resolution in Table 1, i.e., a mesh with (3072, 1536) points.

A key result is the development of an eddy "temperature wake" in the boundary layer interior, see Fig. 16. The field is noisy as only point-by-point time averaging is used to construct the anomaly. Near the ABL top z = 398 m the temperature wake is first visible aft of the eddy center. At z = 28.6 m the magnitude of the anomaly pattern above the eddy is large and exhibits a dipole structure similar to the surface flux pattern in Fig. 12. However, the θ field at z = 28.6 m also exhibits a coherent trailing wake downstream of the eddy. The downstream vertical tilt of the wake between the surface and ABL inversion is a consequence of z-varying horizontal advection. Flow visualization shows the temperature wake persists for at least 5 radii downstream of the eddy. A vertical slice in an y–z plane at x/r_m = 6.875 r_m, shows clear rotation and a persistent secondary circulation generated by the vector field $(v, w)_a$, see supplementary material. Notice the center of the rotation is asymmetric about y = 0 matching the asymmetric heterogeneity in the surface temperature flux, q_s is stronger on the north side of the eddy. The streamtraces are found from anomaly fields averaged over 2.5 km in x. The streamwise anomaly $u_a \sim \mathcal{O}(v_a)$ varies in the y–z plane and the eddy wake is three-dimensional. The structure and coherence of eddy induced wakes in the ABL are a topic for future investigation.

d. *Wind work*

The LES allows us to compute the magnitude and distribution of wind work between the atmosphere and ocean Renault et al. (2016), but with the caveat that the present simulations do not include an active oceanic model for the evolution of the currents. Wind work is the temporal correlation between wind stress–winds and wind stress–currents that appear in depth-integrated energy budget equations for the atmosphere and ocean (e.g., Marchesiello et al. 2003). To expose the eddy impact on air–sea kinetic energy transfer the far-field values of wind work are subtracted from the wind-work anomalies (F_aK_a, F_oK_o). Thus, let

$$F_aK_a = \overline{\boldsymbol{\tau}_s \cdot \mathbf{u}_a} - \overline{\boldsymbol{\tau}_s \cdot \mathbf{u}_a}\big|_f, \tag{25a}$$

$$F_oK_o = -\overline{\boldsymbol{\tau}_s \cdot \mathbf{u}_o} + \overline{\boldsymbol{\tau}_s \cdot \mathbf{u}_o}\big|_f, \tag{25b}$$

where the overbar $\overline{()}$ indicates a time average, $|_f$ denotes wind work in the far field. By construction these anomalies vanish

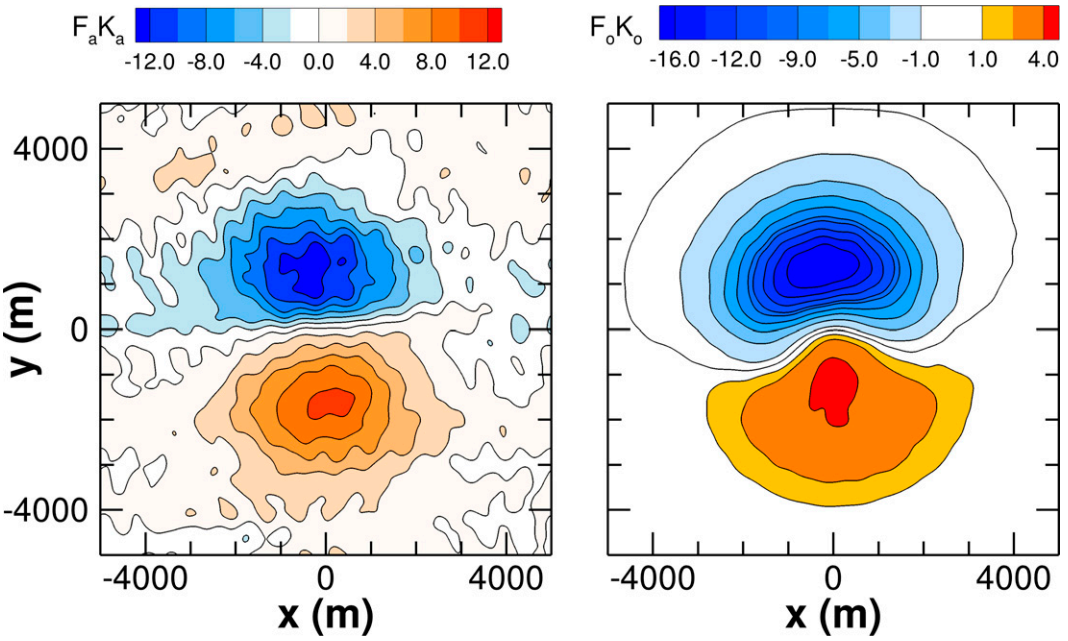

FIG. 17. The eddy components of wind work (F_aK_a, F_oK_o) in (26) normalized by u_*^3 from simulation i03 with a cyclonic eddy with radius $r_m = 2$ km. (left) F_aK_a and (right) F_oK_o are shown. For reference, the normalized average far-field wind work $\overline{\boldsymbol{\tau}_s} \cdot \overline{\mathbf{u}_{1/2}}|_f = -19.6$.

away from the eddy. The opposite sign in F_oK_o assures that positive values in both wind-work expressions have the sense of energy transfer into, respectively, the atmosphere or the ocean. In (25a), the surface wind $\mathbf{u}_a$ is evaluated at the first model level $z_{1/2}$ (Fig. 5). The above correlations are next rewritten in terms of a temporal mean and fluctuation, i.e., $\overline{\boldsymbol{\tau} \cdot \mathbf{u}} = \overline{\boldsymbol{\tau}} \cdot \overline{\mathbf{u}} + \overline{\boldsymbol{\tau}' \cdot \mathbf{u}'}$, resulting in

$$F_aK_a = \underbrace{\overline{\boldsymbol{\tau}_s} \cdot \overline{\mathbf{u}_a} - \overline{\boldsymbol{\tau}_s} \cdot \overline{\mathbf{u}_a}|_f}_{\text{Eddy}} + \underbrace{\overline{\boldsymbol{\tau}_s' \cdot \mathbf{u}_a'} - \overline{\boldsymbol{\tau}_s' \cdot \mathbf{u}_a'}|_f}_{\text{Turbulence}}, \tag{26a}$$

$$F_oK_o = \underbrace{\overline{\boldsymbol{\tau}_s} \cdot \overline{\mathbf{u}_o}|_f - \overline{\boldsymbol{\tau}_s} \cdot \overline{\mathbf{u}_o}}_{\text{Eddy}} + \underbrace{\overline{\boldsymbol{\tau}_s' \cdot \mathbf{u}_o'}|_f - \overline{\boldsymbol{\tau}_s' \cdot \mathbf{u}_o'}}_{\text{Turbulence}}. \tag{26b}$$

The eddy and turbulence contributions to wind work in the atmosphere and ocean are indicated by the underbraces in (26). Because of our posing of this LES problem, $\mathbf{u}_o$ is constant in time; therefore, the turbulence term in F_oK_o is zero.

Contour plots of the eddy contribution to (F_aK_a, F_oK_o) from simulation i03 are shown in Fig. 17, where the fields are normalized by $\rho_a u_*^3$, the natural atmospheric scaling. The time averages at each x–y location are obtained from 22 surface volumes spanning approximately 6000 s. Results are smoothed with a spatial low-pass Gaussian filter with cutoff $\delta = 500$ m. For reference the normalized average far-field atmospheric wind work $\overline{\boldsymbol{\tau}_s} \cdot \overline{\mathbf{u}_a}|_f = -19.6$ and the turbulent contribution $\overline{\boldsymbol{\tau}_s' \cdot \mathbf{u}_a'}|_f = -1.4$; i.e., the atmosphere is losing energy to the ocean through the drag force. The contours in Fig. 17 broadly replicate the surface stress anomaly patterns shown in Fig. 12. Note the larger negative values of F_oK_o on the north side of the cyclonic eddy clearly show the enhanced "eddy-killing" mechanism described by Renault et al. (2016) where the ocean on average is losing its eddy kinetic energy back into the atmosphere. The computed far-field wind work in the ocean for our circular eddy is near zero as expected with no far-field currents. The eddy impact on wind work in the atmosphere is interesting. Inside the eddy, wind work is large with peak values approaching ±50% of the far-field atmospheric wind work, which translates to 0.012 W m^{-2}, a small value compared to the temperature flux anomaly of 4.8 W m^{-2}. Note that the wind work is (from, to) the atmosphere on the (north, south) sides of the eddy. In contrast to the ocean, the (positive, negative) values of wind work in the atmosphere are approximately in balance, and the net wind work is nearly zero. The peak magnitude in $|F_aK_a| \approx 14$ is not very different from the peak magnitude in $|F_oK_o| \approx 19$, and the patterns in both are dipolar.

8. Summary and discussion

High Reynolds-number, large-eddy simulation (LES) is used to examine stratified marine atmospheric boundary layers (ABL) forced by a combination of geostrophic winds and convection above an oceanic eddy of varying radius $r_m = [0.4\text{–}4]$ km; the maximum azimuthal eddy speed is 1 m s^{-1}. The simulations span the unstable regime $-1/L = [0, \infty]$ where L is the Monin–Obukhov (M–O) stability parameter. Eddy currents are coupled to the ABL in the M–O surface flux formulas.

A linearized Ekman model is developed to help guide and interpret the LES. In contrast to the classical Ekman model, the present formulation couples ABL winds to a nonlinear rough-wall stress boundary condition that depends on the air–sea relative velocity $\Delta\mathbf{u}$. As a result, the Ekman model

shows how surface stress develops a dipole anomaly under the action of neutral winds. The dipole is understood as a consequence of surface winds aligned or opposing the surface currents. For a cyclonic eddy the stress anomaly is (positive, negative) in the (north, south) quadrants of the eddy. In good agreement with the Ekman model, the LES also develops a dipole in the surface stress. However, the Ekman model for a cyclonic eddy predicts a strong downdraft magnitude for vertical velocity in the ABL interior which is not found in the simulations. In the absence of an accompanying convective surface flux, the LES predicts weaker downdrafts and an asymmetric w pattern because of horizontal wind advection; the updraft–downdraft pattern for w is reversed for an anticyclonic eddy with neutral winds in both the Ekman model and LES, see sections 2 and 5.

In the free-convection regime (no mean wind), an oceanic eddy with r_m = [0.4, 4] km is particularly impactful on the ABL. A wide vigorous updraft is found above the eddy center and persists over the depth of the ABL. The radial wind is inward at the surface and outward at the ABL top. The azimuthal wind aligns with the eddy rotation either cyclonic or anticyclonic, and there is a positive q_* anomaly in a ring where the current speed is a maximum, as anticipated in the Ekman model. The eddy induces large signals in the ABL temperature and pressure fields, and in the horizontal velocities at the inversion layer. Near the surface smaller downdrafts are arranged in a circular ring outside the central wide updraft at the eddy center; i.e., the ABL organizes its largest updrafts to be inside the ring of enhanced q_*. With fixed sea surface temperature the oceanic eddy generates heterogeneity in surface temperature flux which is mainly responsible for the full ABL impact. A simulation with no currents and specified heterogeneous surface temperature flux predicts a similar ABL response as a simulation with currents and constant specified SST. As discussed near the end of section 2, the neutral Ekman model for no mean wind (i.e., $\mathbf{u}_g = 0$) predicts a central updraft (downdraft) for a cyclonic (anticyclonic) eddy; clearly the surface heat flux feedback in free convection overwhelms this predicted neutral circulation. There is clear cooperative behavior between surface convection and the central updraft induced by anticyclonic eddy rotation; in the region near the eddy core $0 < r/r_m < 1.5$ both the temperature flux and the vertical velocity in the ABL interior are enhanced compared to simulations with a cyclonic eddy, see section 6.

The new feature in the mixed wind and convection regime is the development of a dipole in surface temperature flux that coexists with the surface stress anomaly. Even with fixed (constant) SST a temperature flux anomaly appears because of current coupling $|\triangle\mathbf{u}|$ in the surface flux formulas. The temperature θ_a, pressure p_a, and spanwise velocity v_a anomaly fields are sensitive metrics of an oceanic eddy impact. For large r_m the temperature field is persistently heterogeneous at scales larger than the ABL depth z_i, i.e., $z_i/r_m < 1$. With geostrophic winds oriented in the x direction the surface temperature flux develops persistent gradients $\partial_y\theta_a$, which in turn drive pressure gradients $\partial_y p_a$ near the surface and inversion. ABL winds over an oceanic eddy are in the "alongfront" wind regime Sullivan et al. (2021). Well organized patterns in the spanwise anomaly v_a are found near the surface and at the top of the boundary layer in the low-wind regime with $u_g = 2.5$ m s^{-1} combined with convection at $r_m > 2$ km. The spanwise horizontal scale of v_a matches the variation in the anomaly (θ_a, p_a) fields. Simulations past an isolated eddy develop a downstream "wake" and secondary circulations that fill the boundary layer vertically and persists for more than 5 radii downstream of the eddy. The anomalous wind work associated with the current feedback acts to deplete the oceanic kinetic energy ("eddy killing") but only spatially rearranges the atmospheric kinetic energy balance, see section 7.

In the submesoscale ocean regime with horizontal scales $0.1 < \ell < 10$ km, an ocean eddy impacts the ABL in low-wind convective conditions: Edson et al. (2007) documents typical low-wind conditions. The strength and scale of the induced secondary circulations and modification to the surface fluxes grows with increasing eddy radius and speed. The LES and the linearized Ekman model show the importance of coupling currents in both surface momentum and temperature flux rules. Also, the LES results provide a target for focused surface layer and boundary layer observations with varying atmospheric stability above a heterogeneous ocean. The impact of mesoscale eddies with $r_m > 20$ km using LES and coupled atmosphere–ocean models is a topic for future work.

Acknowledgments. PPS and JCM were supported by the Office of Naval Research through the Physical Oceanography Program Awards N00014-17-1-2334 and N00014-18-1-2599, and by the National Oceanic and Atmospheric Administration Award NA19OAR4310378. PPS acknowledges support from the National Science Foundation and the Geophysical Turbulence Program at the National Center for Atmospheric Research (NCAR). This research benefited greatly from computer resources provided by the Department of Defense High Performance Computing Modernization Program and NCAR's Computational and Information Systems Laboratory (doi:10.5065/D6RX99HX) sponsored by the National Science Foundation.

Data availability statement. Simulation data are available on request.

REFERENCES

Ayet, A., N. Rascle, B. Chapron, F. Couvreux, and L. Terray, 2021: Uncovering air-sea interaction in oceanic submesoscale frontal regions using high-resolution satellite observations. *U.S. Clivar Var.*, **19**, 10–17.

Businger, J. A., 1972: Turbulent transfer in the atmospheric surface layer. *Workshop on Micrometeorology*, D. A. Haugen, Ed., Boston, MA, Amer. Meteor. Soc., 67–100.

Chelton, D. B., M. G. Schlax, and R. M. Samelson, 2011: Global observations of nonlinear mesoscale eddies. *Prog. Oceanogr.*, **91**, 167–216, https://doi.org/10.1016/j.pocean.2011.01.002.

Chen, S. S., J. F. Price, W. Zhao, M. A. Donelan, and E. J. Walsh, 2007: The CBLAST-Hurricane program and the next-generation fully coupled atmosphere–wave–ocean models for hurricane research and prediction. *Bull. Amer.*

Meteor. Soc., **88**, 311–318, https://doi.org/10.1175/BAMS-88-3-311.

Conzemius, R. J., and E. Fedorovich, 2006: Dynamics of sheared convective boundary layer entrainment. Part I: Methodological background and large-eddy simulations. *J. Atmos. Sci.*, **63**, 1151–1178, https://doi.org/10.1175/JAS3691.1.

Deardorff, J. W., 1970: A numerical study of three-dimensional turbulent channel flow at large Reynolds numbers. *J. Fluid Mech.*, **41**, 453–480, https://doi.org/10.1017/S0022112070000691.

Edson, J., and Coauthors, 2007: The Coupled Boundary Layers and Air-Sea Transfer Experiment in low winds. *Bull. Amer. Meteor. Soc.*, **88**, 341–356, https://doi.org/10.1175/BAMS-88-3-341.

Frenger, I., N. Gruber, R. Knutti, and M. Münnich, 2013: Imprint of Southern Ocean eddies on winds, clouds and rainfall. *Nat. Geosci.*, **6**, 608–612, https://doi.org/10.1038/ngeo1863.

Garratt, J. R., 1992: *The Atmospheric Boundary Layer.* Cambridge University Press, 316 pp.

Gaube, P., D. B. Chelton, P. G. Strutton, and M. J. Behrenfield, 2013: Satellite observations of chlorophyll, phytoplankton biomass, and Ekman pumping in nonlinear mesoscale eddies. *J. Geophys. Res. Oceans*, **118**, 6349–6370, https://doi.org/10.1002/2013JC009027.

——, ——, R. M. Samelson, M. G. Schlax, and L. W. O'Neil, 2015: Satellite observations of mesoscale eddy-induced Ekman pumping. *J. Phys. Oceanogr.*, **45**, 104–132, https://doi.org/10.1175/JPO-D-14-0032.1.

Large, W. G., and S. Pond, 1981: Open ocean flux measurements in moderate to strong winds. *J. Phys. Oceanogr.*, **11**, 324–336, https://doi.org/10.1175/1520-0485(1981)011<0324:OOMFMI>2.0.CO;2.

Marchesiello, P., J. C. McWilliams, and A. Shchepetkin, 2003: Equilibrium structure and dynamics of the California Current System. *J. Phys. Oceanogr.*, **33**, 753–783, https://doi.org/10.1175/1520-0485(2003)33<753:ESADOT>2.0.CO;2.

McWilliams, J. C., 2016: Submesoscale currents in the ocean. *Proc. Roy. Soc. London*, **472**, 1–32, https://doi.org/10.1098/rspa.2016.0117.

——, 2020: Oceanic frontogenesis. *Annu. Rev. Mar. Sci.*, **13**, 227–253, https://doi.org/10.1146/annurev-marine-032320-120725.

Minobe, S., A. Kuwano-Yoshida, N. Komori, S. Xie, and R. J. Small, 2008: Influence of the Gulf Stream on the troposphere. *Nature*, **452**, 206–209, https://doi.org/10.1038/nature06690.

Moeng, C.-H., and P. P. Sullivan, 1994: A comparison of shear and buoyancy driven planetary-boundary-layer flows. *J. Atmos. Sci.*, **51**, 999–1022, https://doi.org/10.1175/1520-0469(1994)051<0999:ACOSAB>2.0.CO;2.

Owinoh, A., J. Hunt, A. Orr, P. Clark, R. Klein, H. Fernando, and F. Nieuwstadt, 2005: Effects of changing surface heat flux on atmospheric boundary-layer flow over flat terrain. *Bound.-Layer Meteor.*, **116**, 331–361, https://doi.org/10.1007/s10546-004-2819-z.

Patton, E. G., P. P. Sullivan, and C.-H. Moeng, 2005: The influence of idealized heterogeneity on wet and dry planetary boundary layers coupled to the land surface. *J. Atmos. Sci.*, **62**, 2078–2097, https://doi.org/10.1175/JAS3465.1.

Pope, S. B., 2000: *Turbulent Flows.* Cambridge University Press, 771 pp.

Raasch, S., and G. Harbusch, 2001: An analysis of secondary circulations and their effects caused by small-scale surface in homogeneities using large-eddy simulation. *Bound.-Layer Meteor.*, **101**, 31–59, https://doi.org/10.1023/A:1019297504109.

Renault, L., M. J. Molemaker, J. C. McWilliams, A. F. Shchepetkin, F. Lemarié, D. Chelton, S. Illig, and A. Hall, 2016: Modulation of wind work by oceanic current interaction with the atmosphere. *J. Phys. Oceanogr.*, **46**, 1685–1704, https://doi.org/10.1175/JPO-D-15-0232.1.

——, J. McWilliams, and J. Gula, 2018: Dampening of submesoscale currents by air-sea stress coupling in the Californian Upwelling System. *Sci. Rep.*, **8**, 13388, https://doi.org/10.1038/s41598-018-31602-3.

——, P. Marchesiello, S. Masson, and J. C. McWilliams, 2019: Remarkable control of western boundary currents by eddy killing, a mechanical air-sea coupling process. *Geophys. Res. Lett.*, **46**, 2743–2751, https://doi.org/10.1029/2018GL081211.

Robinson, W. P., P. Chang, E. Chassignet, and S. Speich, 2019: Ocean mesoscale eddy interactions with the atmosphere. U.S. CLIVAR and CLIVAR Workshop Tech. Rep. 2019-2, 22 pp., https://doi.org/10.5065/ebjm-5q77.

Rotunno, R., 2013: The fluid dynamics of tornados. *Annu. Rev. Fluid Mech.*, **45**, 59–84, https://doi.org/10.1146/annurev-fluid-011212-140639.

——, 2014: Secondary circulations in rotating-flow boundary layers. *Aust. Meteor. Oceanogr. J.*, **64**, 27–35, https://doi.org/10.22499/2.6401.004.

Schlichting, H., 1968: *Boundary-Layer Theory.* 6th ed. McGraw-Hill, 748 pp.

Schmidt, H., and U. Schumann, 1989: Coherent structure of the convective boundary layer derived from large-eddy simulations. *J. Fluid Mech.*, **200**, 511–562, https://doi.org/10.1017/S0022112089000753.

Seo, H., A. J. Miller, and J. R. Norris, 2016: Eddy–wind interaction in the California current system: Dynamics and impacts. *J. Phys. Oceanogr.*, **46**, 439–459, https://doi.org/10.1175/JPO-D-15-0086.1.

Sullivan, P. P., and E. G. Patton, 2011: The effect of mesh resolution on convective boundary-layer statistics and structures generated by large-eddy simulation. *J. Atmos. Sci.*, **68**, 2395–2415, https://doi.org/10.1175/JAS-D-10-05010.1.

——, C.-H. Moeng, B. Stevens, D. H. Lenschow, and S. D. Mayor, 1998: Structure of the entrainment zone capping the convective atmospheric boundary layer. *J. Atmos. Sci.*, **55**, 3042–3064, https://doi.org/10.1175/1520-0469(1998)055<3042:SOTEZC>2.0.CO;2.

——, J. C. McWilliams, and E. G. Patton, 2014: Large eddy simulation of marine boundary layers above a spectrum of moving waves. *J. Atmos. Sci.*, **71**, 4001–4027, https://doi.org/10.1175/JAS-D-14-0095.1.

——, ——, J. C. Weil, E. G. Patton, and H. J. S. Fernando, 2020: Marine atmospheric boundary layers above heterogeneous SST: Across-front winds. *J. Atmos. Sci.*, **77**, 4251–4275, https://doi.org/10.1175/JAS-D-20-0062.1.

——, ——, ——, ——, and ——, 2021: Marine atmospheric boundary layers above heterogeneous SST: Alongfront winds. *J. Atmos. Sci.*, **78**, 3297–3315, https://doi.org/10.1175/JAS-D-21-0072.1.